Near-wake observations behind azimuthally perforated disks with varying hole layout and porosity in smooth airstreams at high Reynolds numbers

Raf Theunissen*
Department of Aerospace Engineering
University of Bristol
Bristol, BS81TR, UK
Email: r.theunissen@bristol.ac.uk

Robert Worboys
Department of Aerospace Engineering
University of Bristol
Bristol, BS81TR, UK
Email: r.worboys@bristol.ac.uk

ABSTRACT

Porous disks are commonly encountered in experimental studies dealing with flow through objects such as wind turbines, parachutes and fluidic devices to regulate pressure and/or downstream turbulence. Perforations are typically staggered and only porosity is altered to attain the required disk drag coefficient, despite a documented influence of topology. Few works have reported however to which extent the spatial distribution of the circular perforations affect the mean flow pertaining freestanding disks and for this reason this work presents a first, more systematic study focused on the effect of azimuthally varying hole topology and porosity on disk drag and near-wake characteristics. An experimental

*Corresponding author.

study performed in airflows of negligible freestream turbulence at Reynolds numbers in the order of 10^5 is reported and related to existing literature to ensure reliability. Complementary to drag measurements, near-wake surveys have been performed on a variety of perforation layouts using two component laser Doppler velocimetry and two-component Particle Image Velocimetry. It is shown that minor changes in perforations can cause drastic changes in near-wake flow topology and no perforation layout can be consistently associated with highest drag. Explicit empirical expressions for drag coefficient linked with the simplified topologies considered have been derived.

1 INTRODUCTION

Perforated disks are used in a variety of applications whereby disks are either free-standing or integrated in pipes to regulate flow non-uniformity or pressure drop. When used for blast mitigation Langdon *et al.* [1] ascribed the positive influence of plates with radially distributed perforations to more efficient diffusion of the blast wave. From that perspective Shaaban [2] was able to reduce the ensuing turbulence intensity and pressure loss by merely altering the hole geometry. Malavasi *et al.* [3] on the other hand observed a dependence of the pressure drop across perforated plates in pipelines not only on porosity, but also on hole disposition and number of holes, although no systematic study in terms of ensuing wake or flow physics was performed.

Such a dependency of drag on porosity is also observed when dealing with freestanding perforated plates, whereby the medium is allowed to flow past the plate. For freestanding disks not only the drag is typically of importance, but also the ensuing wake features. Castro [4] investigated the drag of porous plates with staggered perforation patterns as a function of porosity for two Reynolds numbers and reported, as to be initially expected, an increasing drag coefficient with decreasing porosity. The appearance of a recirculation area behind the disks/plates was also suggested, which delays the merging of the outer shear layers. This region, bounded by the object and the outer shear layers originating from the disk/plate rim, is referred to as the near-wake. It plays an active role in subsequent wake development as the more rapid the shear layers are able to interact, the faster self-preservation in mean velocity sets in [5]. Drag and near-wake are inter-related. Morel and Bohn [6], for example, observed a drastic reduction in disk drag when placing a secondary disk in the upstream near-wake and subsequently, perforated plates can also be used to regulate downstream turbulence levels (e.g. [7]).

Perforated plates are most commonly used in wind turbine modeling to simulate the most important wind turbine wake characteristics because they permit flow-through. Com-

mon wind turbine spacings are in the order of 6-9 rotor diameters. The far wake, where azimuthal velocities due to blade rotation are negligible, is thus of importance and here wake characteristics can be suitably replicated using static discs. Gauze or uniformly perforated disks are often used to emulate the numerical actuator disk model [8–10], despite a documented influence of blade-loading (and thus radial variation in longitudinal velocity) on ensuing wake characteristics [11]. Theunissen *et al.* [12] investigated the suitability of several perforated disk layouts containing multiple holes of varying diameter positioned at multiple radial distances as wind turbine analogues and effectively reported a dependency of the wake recovery not only on porosity, but also on the topology of the perforations. At high porosities, jet-like wakes are formed, void of any recirculation [13, 14]. Cannon *et al.* also showed that for a fixed Reynolds number an increase in porosity of a screen disk corresponds to a decrease in the normalized wake deficit [13]. In flow visualization experiments downstream slotted disks, Higuchi [15] observed complex flow structures appearing in identifiable modes and a strong influence of porosity on the overall near-wake topology. These findings confirm that the wake development can be influenced by the near-wake region, which in turn is influenced by the disks porosity. Roberts [16] reasoned that the near-wake is pivotal in the wake flow behind slotted disks and suggested that the drag coefficient of a porous disk is not uniquely determined by the porosity and Reynolds number alone, but also the slot arrangement. Increasing porosity could even lead to drag coefficients higher than that for a solid disk.

Although these studies are indicative of the intricate influence of perforations on disk downstream wake characteristics, to the best of the authors' knowledge, literature focusing on the observable alterations in wake characteristics, and thus also drag coefficient, with circular perforation topology is scarce. Instead, the bulk of literature considers perforated rectangular plates, solid or gauze disks, concentric slotted disks or disks without the presence of outer shear layers. A more systematic study for freestanding disks with circu-

lar perforations as to how and to which level the near-wake and drag coefficient change with varying hole topology remains missing and is the focus of this paper. In particular, an attempt has been made to decouple the effects of Reynolds number, topology and porosity using simplified hole topologies for a range of porosities at constant Re-number and jet-merging, which is common in jet arrays [17], is scrutinized as a potential mechanism to explain the observed variations.

After discussing the experimental setups and disk parameterization, the results of drag measurements performed on a family of perforated disks of varying porosity and perforation topologies are presented. These illustrate the dependency of the drag coefficient of a porous circular disk on the hole topology. Velocity fields obtained through PIV are utilized to visualize the near-wake in terms of structure and complex flow features, highlighting a strong interaction between the outer shear layers and pore jets. LDA measurements are performed along the wake centerline to complement PIV data and enable a classification of the disks. A methodology to obtain spectral information from the limited LDA data is introduced and its application reveals the presence of near-wake oscillations and larger scale vortex shedding.

2 EXPERIMENTAL FACILITY AND DATA REDUCTION

2.1 Disk geometry parameterization

Four geometric features of the disks with constant radius R have been identified to parameterize the hole topologies (Fig.1 and Tab. 1); hole center spacing S is defined as the shortest distance between the centers of two adjacent holes; hole center radius r_p; pore radius h and number of pores N_h. The geometric parameters are related through the following equations:

$$\frac{h}{R} = \left(\frac{\beta}{N_h}\right)^{0.5} \quad \text{and} \quad S = 2r_p sin\left(\pi/N_h\right) \tag{1}$$

These parameters were varied under constant porosity (β), defined as the ratio between the area of the pores and total disk area, to produce a group of six disks (A, B, C, D, E, F) with different topologies of increasing r_p tabulated in Tab. 1. Contrary to the slotted disks in [16] and [18] the perforations were expected to individually produce small jets, which allowed the verification of whether the phenomenon of jet merging, present when dealing with parallel 2D jets [19], also occurs in axially symmetric 3D configurations and is the underlying cause of alterations in near-wake flow topology. The dominant parameter influencing parallel jet merging is the jet spacing to diameter ratio, S/h, and values were repeated across different porosities. The number of holes N_h was selected to be either four or six. These were chosen to provide the lowest number of holes generating a perforation layout with at least two orthogonal planes of symmetry thus preserving as much symmetry as possible. The radius of the holes (h) was determined as a result of obtaining the correct porosity once the number of holes was selected as per Eqn.1. With the focus on identifying jet merging, simplistic topologies were considered with a unique radial location per hole layout for all perforations. This also allowed investigating purely the effect of distancing pores away from the centerline. The hole center radius r_p was varied to enable a matching between the spacing ratio S/h for disks across different porosities as well as varying the radius ratio r_p/R. Disks had a thickness t of 6 mm, yielding a thickness to diameter (D) ratio of 0.1.

2.2 Wind tunnel facilities

Experiments were performed in the low turbulence wind tunnel of the department of Aerospace Engineering at the University of Bristol. This is a closed circuit tunnel capable of speeds up to 100 m/s whilst providing a flow of high uniformity and turbulence intensity levels below 0.09% [20]. The working section has a rectangular cross-section of 0.8 m $\times$ 0.6 m.

For the force measurements disks were laser cut and attached to a load cell, which in turn was fixed to an aerodynamically shaped arm (Fig.2a). A single axis force measurement was permissible as a direct result of the perforated disks' symmetry, with the axes of symmetry perpendicular and parallel to the load cell as elaborated in the appendix. The load cell was equipped with a 5 N capacity strain-gauge (Strain Measurement Devices, SMD2207-005) connected to a 16bit A/D board. With maximum voltages in the order of 0.25 Volt, the bipolar voltage range was set to $\pm$1 Volt yielding a resolution of 2 Volt/2^{16} and equating to a negligible resolution-related uncertainty in voltage readings of $\pm$ 5.66 $\times 10^{-17}$ Volt. A linear calibration between acting force F_C and voltage was obtained F_C =23.58 ($\pm$ 0.15)$\times$Voltage where the uncertainty was defined at 95% confidence level. Since the relative contribution of calibration uncertainty equaled approximately 6.36$\times 10^{-3}$, relative uncertainties in drag coefficients (σ_{C_D}/C_D) would be dominated by uncertainties in voltage readings, which in turn would be dictated by data scatter rather than finite resolution. Deflections of the load cell were negligible (0.2 mm) following the load cell manufacturer's specifications even at 50 m/s (F_D $\approx$3.5 N). Readings were obtained with and without disks to retrieve the drag measurements pertaining solely to the disks. Imposed wind speeds ranged between 10 m/s and 50 m/s to achieve a variation in diameter-based Reynolds number. When performing wake surveys, all disks were subjected to a freestream velocity U_∞ of 30 m/s equating to a diameter-based Reynolds number Re_D =1.2$\times 10^5$. This Reynolds number was selected as drag coefficients were observed to remain constant

with increasing Re_D (Fig.5a). Inside the pores, boundary layers would develop and consequently cause pore blockage to increase with disk thickness, yielding higher resistance coefficients as verified in [21]. Assuming a laminar boundary layer (Blasius solution), in the current study the boundary layer thickness δ at the exit of the pores was estimated to be (U_∞ =30 m/s, ν =15.2$\times 10^{-6}$ m/s) $\delta \approx 4.91\sqrt{\nu t/U}$ =0.27 mm or an equivalent minimum area ratio of $(1-\delta/h)^2 = 0.90$ thus allowing pore blockage to be neglected overall. In wake surveys the disks were 3D-printed out of ABS-M30 for manufacturing practicality and inserted in an aluminum ring (yielding a total diameter of 60 mm) located at the center of the test section. The ring was attached to the test section through four 3mm metallic poles (Fig. 2c). Given their small radius with respect to the disk diameter, the influence of the rods on the wake structure was marginal. The natural frequency of the structure with different degrees of tension applied to the rods was measured in several impact tests and ranged between 31.8 Hz (no tension) and 41.2 Hz equivalent to a Strouhal number $St = \frac{fD}{U_\infty}$ =0.08 (tension). Additional modal contributions were observed at 158.9 Hz and 190 Hz (no tension), and under tension at 180.7 Hz (St =0.3614) and 227.1 Hz (St =0.45). All measurements were performed with tensioned rods. The dominant vortex shedding of a circular disk appears at a Strouhal number St =0.135, signifying resonance of the frame not to influence accrued data. The deflection of the disk normalized by its diameter in response to a static force F_D was found to follow the empirical relation 10.4 ($\pm$1.2) $\times 10^{-3} \times F_D$ with the uncertainty defined at 95% confidence level (CL). With a nominal drag force at 30 m/s of 1.56 N, the (normalized) deflection amplitude was a negligible 16$\times 10^{-3}$. Oscillations of the disks in the direction of the freestream were still present as will be shown in Section 2.4. However, based on PIV recordings the maximum deflection ratio was in the order of only 5.33$\times 10^{-3}$ (5 pixels), which according [22] was too low to modify natural frequencies in the wake.

2.3 Data acquisition

When performing force measurements, for each disk and velocity setting, 1800 samples were collected. To ensure samples were separated by at least twice the flow-related time scales, a sampling frequency of 30 Hz was selected given the objective of retrieving reliable statistical moments [23]. All 1800 samples obtained could thus be considered independent. Accrued data was subsequently analyzed by means of the bootstrapping process described in [24] to return statistical moments and uncertainty estimates at 95% confidence level.

Planar wake velocity fields were obtained using a two-dimensional, two component (2D2C) Dantec Dynamics Particle Image Velocimetry (PIV) system (Fig.2d). For each disk tested with PIV, three orientation measurement planes were taken consecutively; a vertical plane crossing two pores, a diagonal plane between pores and an offset plane across two pores (Fig.3). While the former allowed visualization of pore jets merging along the centerline, the latter revealed the possible merging of jets with their nearest neighbor. Seeding was generated by atomizing a mixture of PEG-80 and water producing tracer particles with a mean diameter of 1 μm. Illumination was provided by a Litron 200 mJ laser with a repetition rate of 15 Hz and optically transformed into a 1 mm thick laser sheet. This sampling frequency ensured all velocity fields to be statistically independent. The CMOS sensor of the SpeedSense M340 consisted of 10 μm pixels arranged in a 2560$\times$ 1600 pixels^2 array. With a calibration factor k of 15.5 pixels/mm, the corresponding field of view covered approximately 2.75 disk diameters downstream and 1.72D in the vertical direction. The calibration factor was obtained by imaging a calibration target and enabled the standard deviation in calibration to be estimated ($\sigma_k = 0.02$ pixels/mm). The separation between laser pulses was set at δ_t =40 μs, producing a maximum particle image displacement, $(\delta_x)_{max}$, of approximately 20 pixels at the pores. Images were *a-priori* enhanced using a minimum intensity background subtraction followed by a spatial low-pass filtering adopt-

ing a Gaussian kernel with 1 pixel standard deviation. In total 1936 image recordings were analyzed with a standard PIV processing routine incorporating iterative correlation window size reduction and image deformation [25]. Final correlation window sizes were 32 pixels$\times$32 pixels ($\approx$ 2.1 mm $\times$ 2.1 mm) with an overlap of 75% resulting in a structured vector field with approximately 0.52 mm grid spacing. The standard deviation in obtained correlation estimates σ_{δ_x} (or random measurement error), which is inherent to the image processing, was estimated at 0.10 pixels based on standard literature [26]. The velocity u expressed in m/s was evaluated as $u = \delta_x/(k \times \delta_t)^{-1}$. Accordingly, symbolizing the spread in the velocity by σ_u, the combined relative uncertainty was retrieved through the standard process $\left(\sigma_u/u\sqrt{1936}\right)^2 + \left(\sigma_{\delta_x}/\delta_x\right)^2 + \left(\sigma_k/k\right)^2$. The largest value of σ_u across the disks considered in the PIV experiments was observed near the pore jets for the case of $\beta = 0.25$, topology E, for which $\sigma_u = 20.79$ pixels and $\delta_x = 14.53$ pixels. Accordingly, the maximum relative uncertainty at 95% confidence was calculated to be 6.52%.

Wake velocities along the disk centerlines were characterized using a Dantec Dynamics two-component Laser Doppler Anemometry system (LDA) equipped with a 600 mm focal length lens (Fig.2b). Denoting the downstream distance by X (Fig.3), sampling was conducted with a resolution of 0.05D (3 mm) between $0.3 \leq X/D \leq 4.3$ (86 locations) and 0.17D (10 mm) between $4.3 \leq X/D \leq 8.3$ (25 positions) giving a total of 111 measurement locations. The initial non-zero measurement location was due to the disk mounting structure unavoidably obstructing the laser paths (Fig.2b). The principle beams had a diameter of 2.2 mm and were separated 38 mm prior to passing through a beam expander of ratio 1.98. This yielded maximum measurement volume dimensions of 0.179 mm and 2.8 mm perpendicular and parallel to the flow direction respectively. The two orthogonal planes spanned by the two laser beam pairs were orientated at an angle of 45 $^\circ$ with respect to the freestream direction to maximize the data rate in coincident mode (coincident mode refers to the validation of a burst signal only when the signal recorded by all

LDA channels, i.e. directions, is considered valid simultaneously). The laser probe was mounted on a computer controlled traverse system capable of incremental displacement steps of 0.5 mm. At each spatial sampling location, typically 8000 instantaneous measurements (N =8000) were collected at a data rate of 0.8 kHz. Transit times, Δt_m, defined as the difference in tracer particle arrival times, were used as weighting in the calculation of statistical moments (mean, $\overline{u}$ and variance, $\overline{u'^2}$) to reduce bias errors [27];

$$\overline{u} = \frac{\sum_{i=1}^{N} u_i \Delta t_i}{\sum_{i=1}^{N} \Delta t_i} \quad \text{and} \quad \overline{u'^2} = \frac{\sum_{i=1}^{N} (u_i - \overline{u})^2 \Delta t_i}{\sum_{i=1}^{N} \Delta t_i} \tag{2}$$

2.4 Data reduction

To rule out potential deviations in drag coefficients caused by variations in wake-blockage, a correction in line with [28] and [29] was adopted. Regarding the LDA data, turbulent spectra can be derived though such routines require the number of recordings to be extensive (e.g. [30, 31]). Given the number of measurement locations, the focus in the present work therefore is not characterization of turbulence, but extraction of dominant lower flow frequencies (the spectral range covering vortex shedding) for which a simplistic, yet reliable procedure is preferred. For this reason the residence-time weighted burst-mode method as proposed in [32] has been implemented.

A frequency resolution $\Delta f = (f_{\max} - f_{\min})/K$ was imposed, where the minimum and maximum frequencies considered, $f_{\min}$ and $f_{\max}$, were selected as 0.1 Hz and 10^3 Hz respectively. The number of frequencies K was related to the overall record time T_{rec} and a typical value Δt for the transit times by $K = T_{rec}/\Delta t$. The transit time scale Δt was calculated as the median of all transit times yielding typical values for K in the order of 10^3. The accrued data (for each sampling location) was partitioned into 10 ($B = 10$)

blocks. For each block the transit time weighted mean and fluctuating velocity were evaluated following Eqn. 2. Denoting N_b as the number of data points in the b^{th} block, T_b the corresponding temporal length of the block and the conjugate operation by $(\cdot)^*$, the block averaged spectral amplitude $S_{u,k}$ related to the horizontal velocity component (u) for a frequency f_k ($k = 1, \ldots, K$) was calculated as;

$$S_{u,k} = \frac{1}{B}\sum_{b=1}^{B} \frac{|W_{b,k}W_{b,k}^*|}{\left(\sum_{n=1}^{N_b}\Delta t_{n+(b-1)N_{T,b}}\right)^2} T_b \tag{3}$$

where $N_{T,b} = \sum_{m=1}^{b-1} N_m$ and $W_{b,k} = \sum_{n=1}^{N_b} e^{-2\pi i t_{n+(b-1)N_{T,b}} f_k} u(t_{n+(b-1)N_{T,b}})\Delta t_{n+(b-1)N_{T,b}}$

The spectra related to v ($S_{v,k}$) were obtained by merely exchanging u and v in Eqn. 3. Resulting spectra for the solid disk at $X/D = 1.0$ and 2.5 are presented in Fig.4a. Spectra below a diameter-based Strouhal number of approximately 0.01 depicted unphysical drops inherent to the involved data analysis process and have been discarded.

For a given disk, the dominant spectral peak in each velocity component was extracted at each of the 111 downstream locations (Fig.4b). A probability distribution was then constructed from the 111 peak frequencies adopting the average shifting histogram (ASH) technique discussed in [33] (Fig.4c). Considering the horizontal velocity component u and defining $\kappa_0 = ((u)_{\max} - (u)_{\min})/(1 + \log_2(N))$, the appropriate m was sought to ensure the number of sub-bins, $n_{bin} = \lceil (2 + 2^{-m}\kappa_0) \rceil$, exceeded 400. The resulting sub-bin width was subsequently given as $\kappa = 2^{-m}\kappa_0$ with the bin centers ranging from $(u)_{\min} - \kappa$ to $(u)_{\max} + \kappa$ in steps of κ, returning a corresponding bin count θ_k ($k = 1, \ldots, n_{bin}$). A biweight kernel function $\phi(t) = \frac{15}{16}(1 - t^2) + 2$, where $(x)_+$ attains the value x provided $x \geq 0$ and 0 otherwise, was utilized to yield the weights w_m allowing the evaluation of the average

shifted histogram $\theta_{ASH,k}$ at the corrected bin centers $(u)_{\min} + (k - 0.5)\kappa$:

$$\theta_{ASH,k} = \frac{1}{N\kappa_0} \sum_{j=max(1,k+(1-m))}^{j=min(n_{bin},k+(m-1))} w_m(j-k)\theta_j \quad \text{with} \quad w_m(i) = \frac{m\phi(\frac{i}{m})}{\sum_{j=1-m}^{m-1}\phi(\frac{j}{m})} \tag{4}$$

The output of these routines is exemplified in Fig.4c. In the local vicinity of maxima, the probability density function (pdf) in observed Strouhal numbers was assumed to follow a normal distribution. As such, the width of the pdf at 75% of the peak value amplitude (Fig.4c) allowed the uncertainty in the Strouhal number dominating the flow at 95% confidence level to be derived as 1.292 times the determined width; let pdf$(St) = \exp(-St/2\sigma_{St}^2)$, then width $= 2\sqrt{-2\log_e(0.75)}\sigma_{St} = 1.52\times\sigma_{St}$ and $1.292\times$width $= 1.96\times\sigma_{St}$. A 75% peak amplitude was selected as the curve bounds for smaller amplitude ratios were generally not well captured.

3 RESULTS AND DISCUSSION

3.1 Drag coefficient versus porosity

The evolution in wake-blockage-corrected drag coefficient with Reynolds number for a selection of disks is depicted in Fig.5a. Drag coefficients can be seen to attain nearly constant values beyond $Re_D = 1.25 \times 10^5$, with reminiscent fluctuations within the uncertainty bands. The reported drag coefficients are valid for a smooth freestream (less than 0.09% turbulence intensity) and can be expected to increase with freestream turbulence intensity [34].

Drag values as a function of porosity are tabulated and illustrated in Tab. 2 and Fig.5b respectively. It is clear that porosity is the dominant factor in the variation in drag coefficient. The drag coefficient for a solid disk was measured at 1.167, which is within the

typical range between 1.11 and 1.17 for Reynolds numbers of 1.3×10^5 [35]. As reported by Roberts [16], careful selection of porosity ($< 10\%$) and pore topology may yield drag coefficients exceeding that of the solid disk, and indeed the disk topologies at a lower porosity of 5% and 10% can produce drag coefficients greater than that of a solid disk. Figure 5b also incorporates the drag equation proposed by Taylor [36] relating the drag coefficient of a screen disk to porosity; $C_D = p/(1 + \frac{1}{4}p)^2$ with $p = (\beta^{-1} - 1)^2$. While this simplistic equation provides a reasonable fit for higher porosities, it is only valid for porosities in excess of $1/3$. The dashed line in Fig.5b on the other hand represents an empirical fit to the present data and captures the typical tendency of increasing drag coefficient with decreasing porosity;

$$C_{Dfit} \approx (\beta^{-1} - 1.62) \times (0.1 + 0.87 \times (\beta^{-1} - 1.52))^{-0.975} \tag{5}$$

While providing a good fit to the measured data, the curve becomes unreliable for $\beta < 5\%$ as it incorrectly predicts the gradual recovery in drag coefficient with porosity towards the value of a solid disk ($\beta^{-1} \to \infty$). The authors would like to stress that the curve only represents a global fit to the measured drag coefficients and does not take into account the data scatter for a given porosity.

Measured drag coefficients are noticeably scattered around the empirical trendline. Craze [34] stipulated that for a bluff body with relatively fixed separation point, which in the case of a solid disk will be on the outer perimeter, the drag coefficient is controlled by the behavior of the outer free shear layer. In particular, the characteristic thickness, entrainment length and velocity just outside the shear layer are the dominant parameters, which in turn are influenced by the turbulence levels in the air stream and bluffness of the body. Since

the shear layer will be turbulent once separated, the length of the entrainment region, and the majority of near-wake characteristics for that matter, are expected to be Reynolds number independent. This further justifies limiting the performed investigations to a single (sufficiently high) Re_D and, given the low turbulence intensity of the wind tunnel used, implies the observed drag diversity in this study to be solely due to modifications in the disks (i.e. bluffness). With error bars indicating 95% confidence levels, the depicted variation in drag coefficient for a given porosity cannot be explained by measurement data scatter (nor blockage correction inaccuracies) and is consequently ascribed to underlying flow dynamics, i.e. the near-wake.

Based on the provided data, for a given porosity (Tab. 2) no single topology (A-F) can be assimilated with highest drag. Topology E does consistently produce the lowest drag coefficients though and it is exactly for this layout that the spacing between the disk and pore edges, $1-(r_p+h)/R$, is lowest. Hence, it can be concluded that the interaction between pore jet and shear layer plays a dominant role and is influenced by the pore location. As porosity increases, the highest drag coefficient is also attributed to topologies with increasing r_p, thus more rapid interaction with the outer shear layer as visually evidenced in the PIV results (Section 3.2.). Conversely, it is not the topology with the largest $1-(r_p+h)/R$ values (i.e. topology B) that produces the largest C_D. This implies that neither the pore spacing $(S-2h)/R$, S/h, r_p, h nor N_h individually determine the overall behavior of the drag coefficient, but all parameters combined influence C_D.

3.2 3D wake topology

As a result of the complex interplay between geometrical parameters and ensuing wake, each topology will undoubtedly generate a different wake behavior depending on porosity. To gain deeper understanding of the flow field, PIV measurements behind selected disks are combined in a 3D layout and mean flow fields are depicted in Fig.6-8.

Extracted velocity profiles are presented in Fig.9.

The temporal average of the solid disk wake is well known to display the presence of a single region spanning the azimuthal direction. The porous disks on the other hand have a different wake structure containing two recirculation zones (Fig.6-8); one smaller attached to the disks rear side and positioned in the region between the outer disk rim and pore, and one at a distance from the disk face and bounded by the outer shear layer. The smaller recirculation region is present, independent of the appearance of a secondary stagnation point. The disks with $\beta = 0.05$, topology D and $\beta = 0.10$, topology F (Fig.6,7) for example, will be shown not to exhibit a second stagnation point (Fig.10), but can be seen to have a zone of rotating flow near the disk. For the largest porosity tested ($\beta = 0.25$) the flow topology is no longer reminiscent of that of a solid disk (Fig.8). Instead the near-wake is dominated by two recirculation zones positioned quasi-radially rather than longitudinally. In addition, for the larger porosities tested, jet merging becomes more probable due to the smaller jet spacing. The smaller recirculation zone is bounded by the pore jets and in case of $\beta = 0.05$ forms a first stagnation point along the centerline for topology A. Moving the holes outwards (Fig.6), i.e. $\beta = 0.05$, topology D, the zone reduces in size and the first stagnation point disappears. In both cases ($\beta = 0.05$, topologies A and D) the jets bend outwards towards the outer shear layer.

Increasing the porosity to $\beta = 0.10$, larger-scale changes in the structure of the near-wake are minimal as two larger recirculation zones can still be identified (Fig.7). The extent of the near-wake region does not alter dramatically: from 2.43 diameters to 2.28 D (Tab. 3), but the momentum through the pores increases (Fig.11) and the stagnation point nearest to the disk, if present, is moved from 0.5-0.6 D to 1.2 D downstream. As a result, the wake area is more deformed: the wake diameter is visually reduced, the center of the furthest recirculation zone is moved downstream and closer to the centerline and a much smaller tertiary recirculation zone, which exhibits azimuthal symmetry, is formed at a downstream

($X/D \approx 0.6$) and radial distance nearly equal to the disks radius. In addition, streamlines can be seen to converge towards the centerline indicating jet merging. Also for $\beta = 0.10$ increasing the radial position of the pores leads again to the disappearance of the stagnation point closest to the disk as the pore jets rapidly bend outwards to interact with the outer shear layer.

Enlarging the pores (increasing porosity) leads to either a loss in axial symmetry (Fig.8) or the absence of a well-defined near-wake. For the largest porosity considered in the PIV experiments, pores are of sufficient size to make the disk no longer act as a bluff body. For $\beta = 0.25$, topology E a stagnation point is still formed, but the recirculation zones are bounded by the outer shear layer and pore jet, and the jet and centerline. The near-wake region is clearly reduced in size and yields a lower drag coefficient (Tab. 2). While in Fig.8d-f the pore jets bend outwards to interact with the shear layer, bringing the pores closer (Fig.8a-c) causes the jets to bend inwards creating a single jet of sufficient momentum to destroy the typical encapsulated near-wake region. Nevertheless, axial symmetry is preserved.

The PIV measurements show the wake of the perforated disks to be generally quasi-axisymmetric, with the centerline being the axis of symmetry as the wake structure is relatively unchanged moving between the vertical and diagonal planes. Topology E for $\beta = 0.25$ (Fig.8) shows to be an exception, as the bisecting plane between the pores no longer shows the presence of recirculating flow between the disk outer rim and pore. The alteration in near-wake in response to changing the topology for a fixed porosity is shown to be dependent on the porosity itself and no general behavior can be identified.

Details of the wakes in the form of longitudinal velocity profiles extracted in the vertical and across PIV planes are provided in Fig.9. For $X/D < 1$ across the outer shear layers the longitudinal velocity can be seen to change sign for all disks. With values of $U/U_\infty = 1$ indicating the freestream region, the profiles reveal that for disks $\beta = 0.05$, topology A and

D these shear layers are pushed furthest outwards and the least for porosities of $\beta = 0.25$, topologies A and E. Once pore jets are absorbed in the outer shear layer, all velocity profiles become similar and display a qualitative behavior equal to that of the solid disk, i.e. a bluff body. Differences between the disks are thus concentrated within the near-wake and disks can sequentially exhibit an initial reverse flow along the centerline, which in the vertical plane (Figs.9a,c) gradually dampens out with downstream distance (e.g. $\beta = 0.10$, topology F, $\beta = 0.25$, topology E), streamwise flow, which develops into reverse flow before termination of the near-wake (e.g. $\beta = 0.05$, topology A, $\beta = 0.10$, topology B) or an increasing backflow followed by gradual transition towards streamwise flow direction (e.g. solid disk and $\beta = 0.05$, topologies A and D). In the across plane these disks all display an initial deceleration of the longitudinal flow component as the measurement plane crosses the curved pore jets, followed by a damping of the reverse flow with downstream distance. Disk $\beta = 0.25$, topology A shows no sign of reverse flow at all on the other hand.
Observing the local peaks in velocity, which are associated with the pore jets, it becomes evident that, with exception of $\beta = 0.10$, topology B and $\beta = 0.25$, topology A, all jets deviate outwards, even in the offset planes. Once merged, the combined nozzle momentum for $\beta = 0.10$, topology B is insufficient to maintain the outer shear layers separated contrary to $\beta = 0.25$, topology A for which a *closed* near-wake region is absent. The profiles reveal that even though pores were generally spaced closer in the across plane, merging did not take place in this plane unless also in the vertical one. For the disk layouts tested, pore jet merging therefore did not happen solely between two neighbouring pores, but included all pores simultaneously and was directed towards the centerline.

3.3 Temporal disk centerline velocity averages

Of the original 30 disks, all porosities up to and including $\beta = 0.25$ were selected for further LDA measurements as these indicated the largest variation in drag across the

topologies. Although both longitudinal and transverse velocities were measured, the latter showed marginal differences with a zero value in the time-average (maximum amplitudes of 0.01m/s), and are therefore omitted from further analysis.

Analysis of the centerline velocity deficits in longitudinal direction, defined as $\frac{\Delta u_m}{U_\infty} = 1 - \frac{U}{U_\infty}$, with normalized downstream distance X/D indicates the presence of five general tendencies across the different topologies, which are depicted in Fig. 10. It should be noted that for all measurements a stagnation point is expected at the disk interface, i.e. $\lim_{X/D \to 0} \frac{\Delta u_m}{U_\infty} = 1$, although the related measurement was inhibited by the experimental configuration (see Section 2.3).

The first category (Fig.10a) involves the presence of a large recirculation area ($\Delta u_m/U_\infty > 1$), which is only obtained for the lowest porosity ($\beta = 0.05$) and for those disks where the pores are located at $r_p/R > 0.41$ (Tab. 1). The solid disk also belongs to this category. Among the four topologies C, D, E, F, differences become marginal beyond 2-3 disk diameters. Indeed, the rear-stagnation point, identifiable as $\Delta u_m/U_\infty = 1$, indicates the location where the outer shear layers merge and the near-wake terminates. The decay in wake velocity deficit of the perforated disks beyond the stagnation point is less rapid than that of the solid disk though, which also displays the largest magnitude in velocity deficit.

In the second regime (Fig.10b) the flow tends to initially have a velocity lower than freestream ($\Delta u_m/U_\infty < 1$) and gradually decelerates (increase in Δu_m) to give rise to an isolated recirculation zone after which ($X/D > 2.5$) the bulk wake starts to recover. This gives rise to an extraordinary mean flow topology consisting of a double stagnation point (see also Fig.6-7). Differences between the different topologies are again mainly limited to the near-wake region ($X/D < 2.5$) and only porosities $\beta = 0.05$ and $\beta = 0.10$ fall within this category, yet in both cases only for topologies A and B. These topologies are associated with the smallest pore edge distances ($S - 2h/R$) within each of the two porosity groups. The pore edge distance is not the determining factor though, as the disk with $\beta = 0.25$

and $S - 2h/R = 0.1$ (topology F), which is the same as pore separation as the disk with $\beta = 0.10$ and topology B, falls in the third category (Fig. 10c).

The third flow regime is predominantly encountered for a porosity of 0.1 and is characterized by a large recirculation area formed directly behind the perforated disk. Velocities in the recirculation zone are quasi-constant, fluctuating around $\frac{\Delta u_m}{U_\infty} \approx 1.3 - 1.4$, contrary to those depicted for the fourth regime (Fig.10d) where the magnitude of the reverse velocity component gradually decreases with downstream distance. This fourth regime is mainly ascribed to the disks with a porosity of 0.2.

Finally, when $S - 2h/R \leq 0.1$ a fifth regime categorizes disks where the flow generally displays no recirculation at all. The outer shear layers do not merge as this event would be identifiable by the appearance of a stagnation point ($\Delta u_m/U_\infty = 1$). Instead, flows emanating from the pores rapidly coalesce into a central jet (see Fig.8). The point where the shear layers of the jets meet, is characterized by a zero velocity in longitudinal direction [37]. This point falls upstream of the current measurement domain and must be consequently located in the very near vicinity of the disk, indicative of almost immediate jet merging upon exit of the pores. Indeed, these disks feature very small pore separations. As the jet edges have merged, the velocity starts to increase (decreasing Δu_m) reaching a maximum between 0.5 and 0.6 disk diameters downstream. This maximum indicates the combine point, i.e. the location at which the axes of the jets merge [19]. Here the pore separation $S - 2h/R$ shows to be pivotal as the velocity deficit at the combine point decreases (equivalent to an increase in local velocity magnitude) with decreasing separation. In the case of $\beta = 0.25$ topology A ($S - 2h/R = 0.01$), the separation is sufficiently small to create a pocket of flow with a higher speed than the freestream ($\Delta u_m < 0$). Once combined, the unified jet momentum gradually decreases only to be re-accelerated at approximately 1.0-1.1 diameters downstream by the higher freestream velocity. Surprisingly, in case of the disk with $\beta = 0.10$ and topology B, of which the evolution in longitudinal

centerline velocity shows typical signs of jet merging, the deceleration can go as far as reverse flow.

It is noticeable that within each porosity group, topologies C, D, E and F demonstrate similar centerline velocity evolutions as do topologies A and B. Local peaks in Δu_m are consistently attained in the vicinity of $X/D \approx 0.5$ and increase in magnitude with r_p. However, the data corroborates that no unique correlation exists between centerline velocity evolution and solely topology, porosity or drag coefficient. A general classification of the disks in terms of flow regime can neither be established on the basis of a single geometrical parameter. Instead small changes in perforations can lead to drastic modifications in flow topology (e.g. $\beta = 0.20$, topology A versus $\beta = 0.20$, topology C).

Figure 10f and Tab. 3 present an overview of the near-wake extents in terms of the shear layer merging point, which is defined as the location where the longitudinal velocity reaches zero ($\Delta u_m / U_\infty = 1$). Among each porosity group a large variation in the location of the merging or stagnation point can be noted and a direct correlation between wake extent and drag coefficient is not evident. Topologies where the pores are located closer to the disk rim seem to produce the largest wake extents, although topology F, for which the pores are distanced furthest from the centerline, is not consistently assimilated with the furthest stagnation point. For parallel jets several studies report a linear dependence between the jet merging point and the jet spacing [19, 38, 39]. Based on the geometrical parameter $S - 2h$ (Tab. 1), such a linear tendency cannot be observed here. Instead a quadratic dependency on porosity shows to be more representative. Following the analysis of Nedic *et al.* [40] the drag coefficient scales proportional with the mean dissipation of turbulent kinetic energy in the wake and the wake volume. When introducing pores, the ensuing jets will augment the mean dissipation. Attaining a drag coefficient lower than a solid disk thus requires the wake volume to be reduced, which is corroborated by the generally shortened wake extents. However, for $\beta < 0.10$ drag coefficients exceed those

of the solid disk, implying lateral extents of the wake to be enlarged for these porosities. Clear signs are indeed visible when comparing the streamline pattern from Figs.6-8 and the velocity profiles in Fig.9.

3.4 Temporal pore centerline velocity averages

Based on the LDA measurements performed on the perforations centerline nearest to the disks ($X/D = 0.3$) the variation in exit velocity u_p is plotted in Fig.11. While for a single jet the measurement location would still fall within the potential core, velocities measured at $X/D = 0.3$ behind the perforated disk are expected to slightly vary from the jet core velocities as jet trajectories are most likely curving either towards the inside or outside at the measurement location [41]. Nevertheless, established tendencies will remain indicative of the envisaged relationships between the disk parameters.

Exit velocities can exceed the freestream velocity U_∞ although no topology can be consistently attributed to the highest u_p and variations in u_p, for a given porosity, are within the error bands. A clear dependency on porosity is present in Fig.11 though as the pore exit velocity increases proportional to $\beta^{0.5}$. Topologies E and F generally seem not to follow this trend, which is most likely caused by the jets having curved too strongly rendering the measurements unrepresentative (i.e. measurement locations were no longer positioned in the jet's core flow). Indeed, topologies E and F are the disks with the perforations distanced furthest from the centerline and are thus expected to interact more rapidly with the outer shear layers. In addition, these topologies can be seen to be assimilated with the highest velocity fluctuations as indicated by the error bars, which is most likely caused by the measurement location to be within the jet shear layer as a result of the outward curving of the jet (Figs.6-8). Excluding topologies E and F, the scatter in mean exit velocity around the trendline within a porosity group is observed to reduce with increasing porosity.

3.5 Near-wake pumping and vortex shedding

Information regarding wake flow periodicity was obtained by analyzing the spectral content of the instantaneous LDA samples as discussed in Section 2.4. The general behavior of the data presented in Fig.4 for the solid disk is representative for all the disks. For the vertical velocity component the probability density function indicates the presence of two dominant frequencies with, for the solid disk, corresponding Strouhal numbers of $St \approx 0.132$ and $St \approx 0.038$, which is in close agreement with the numerical simulations in [42]. The former frequency is well-known and attributed to the regular vortex shedding [43] and can be observed throughout the measurement domain (Fig.4b). Only in the very near vicinity of the disk ($X/D < 1$) do spectral peaks appear which are linked to the pumping motion, i.e. regular shrinking and enlarging, of the near-wake region with a typical frequency of $St = 0.05$ [22, 44, 45]. The present findings that the near-wake is therefore governed by both large and low frequency motion corroborates the findings reported in [46], where a Strouhal number of 0.035 was attributed to the low frequency peak. Whereas the foregoing related studies utilized single wire hot-wires, making it impossible to distinguish contributions from the individual flow components, the present results indicate that the near-wake oscillations of solid or perforated disks are predominantly observed in the vertical velocity component. This absence of distinct spectral peaks related to shear layer instabilities when based on longitudinal velocity along the centerline is in agreement with the numerical simulations presented in [46].

The evolution in identified Strouhal number peaks with porosity for the different disk layouts based on the horizontal St_u and vertical velocity component St_v is depicted in Fig.12. The size of the markers is related to the likeliness of occurrence, i.e. the ratio between the probability of the identified peak frequency relative to the highest probability peak for the tested disk as illustrated in Fig.4c. It should be noted that given a typical extent of the recirculation zones of $2.5D$, the adopted sampling (Section 2.3) yielded an equal share of

peak frequencies representing the near-wake region and outside. This in turn permits the applied scaling based on probabilities.

For the case of the solid disk a dominant St_u of 0.012 ($f \approx 6Hz$) can be observed (Fig.12a). A slight increase in Strouhal number can be observed with porosity, although the St_u remains in the order of $0.01 - 0.02$. Yang *et al.* [42] have reported the occurrence of low frequency oscillations in the order of $St = 0.02 - 0.03$ in the near-wake region for a solid disk. The frequencies observed here are smaller, but are in agreement with [47] and [48]. Without doubt, the observed Strouhal numbers are too low to be due to related to vortex shedding from the mounting rods; following [49], at a Reynolds number based on the rod diameter of approximately 5900, vortex shedding appears at a related Strouhal number of 0.2062 or, in terms of the disk diameter, a Strouhal number $St_u = 0.2062 \times \frac{60}{3} = 4.12$. Moreover, pore Reynolds numbers were above 4000 and sufficiently large to exclude the potential appearance of self-sustained oscillations of the pore jet merging distance [39, 50] or to relate the St_u to interactions between the pore jets [41,51]; in [41] an empirical relation between the shedding frequency, jet spacing and jet exit velocity was derived. Referring to the geometrical parameters in Tab. 1, this relationship can be rewritten as $\frac{fD}{U_\infty}\frac{SU_\infty}{2Ru_p} = St\frac{SU_\infty}{2Ru_p} = C_1 + \frac{C_2}{u_p}$ where the empirical constants C_1 and C_2 varied between 0.243-0.334 and 0.017-0.347 respectively. Utilizing the observed tendency in Fig.11, this yields Strouhal numbers two orders of magnitude larger than the observed St_u in the current study. Therefore the current authors ascribe the low frequencies, which are in the order of 6Hz, to remaining small longitudinal oscillations of the disk mounting structure.

For porosities $\beta = 0.10$ (topologies B, C, D), $\beta = 0.20$ (topologies D, F) and $\beta = 0.25$ (topologies D, E) the probability density functions showed extrema at additional frequencies. As can be verified from the size of the markers in Fig.12a, the likelihood of occurrence of the associated peaks is negligible and these can subsequently be associated

with sporadic outliers in detected peak frequency. Overall, based on these measurements performed at a radial distance $r/D = 0$, no signs of vortex shedding mechanisms can be detected in the spectral signature of the longitudinal velocity component.

Observing the most probable Strouhal numbers based on the spectral analysis of the vertical velocity component however, multiple peaks are detected for all tested porosities. The lower frequency mode in the vertical velocity component is attributed to the near-wake pumping ($St_v \approx 0.038$). This is present for all disks and is fairly constant despite some variations, which remain within the error bands, in each porosity group. Previous studies on parallel planar jets on the other hand have reported the appearance of periodic events whereby the periodicity decreases with increased jet spacing [41]. In the case of the perforated disk, the smallest spacing between pores is given by $S - 2h$ with the pore radius h related to porosity as $\beta^{0.5}$ (Eqn.1). Increasing porosity would thus imply a reduction in spacing and lead to a larger frequency fluctuation, which is not observed here. Despite the pores, the pumping behavior is thus not dictated by the interaction of the jets. However, the pore jets can bend outwards and interact with the outer shear layers. In fact, the frequency related to vortex shedding does show a dependency on porosity in line with findings of Castro [4], following a near-quadratic tendency.

Disks with no rear-stagnation point (Fig. 10e); $\beta = 0.20$ topology A, $\beta = 0.25$ topologies A and C, do not follow this tendency and instead display additional genuine peaks at higher Strouhal numbers. For $\beta = 0.20$ and $\beta = 0.25$ the highest Strouhal number peaks fell within the band related to the natural frequency of the test rig and can be discarded as being flow-related. These disks therefore do not show signs of regular vortex shedding. In addition, despite the absence of a well-defined near-wake region due to the absence of a downstream stagnation point, these disks do contain a recurring low-motion frequency. This suggests the merging of the inner pore-jets, which on average creates this absence of a stagnation point, does not take place constantly, but is one of several flow ”modes”.

Other modes can exhibit the pore-jets merging with the outer shear layers, creating an enclosed near-wake and consequently manifesting a near-wake pumping. The presence of such multiple near-wake patterns has also been reported in [18] for the case of slotted disks and bluff body wakes e.g. [52, 53].

3.6 Drag dependency on disk parameters

Following the previous analyses, no dominant geometrical parameter describing the hole layout could be identified to predict the drag coefficient or wake streamline pattern. Instead a complex interplay between outer shear layer and pore jets was observed giving rise to unpredictable near-wake topologies. Here a strong correlation with the radial location of the pores was noted and for non-dimensional pore spacing $(S-2h)/R$ below 0.1 the jets would merge. Actuator disk theory relates the drag/thrust coefficient to the velocity u_D at the disk as $C_D = 4\frac{u_D}{U_\infty}(1-\frac{u_D}{U_\infty})$. The velocity u_D will be influenced by the flow exiting from the pores and as such the number of pores N_h, their related Reynolds number $Re_p = \frac{u_p h}{\nu}$ and exit velocity u_p. Pore exit velocities could exceed freestream values and showed a square-root relation with porosity ($u_p \propto \beta^{0.5}$, Fig.11). In turn, a relationship can be expected to exist between these variables and the drag coefficient of the perforated disks.

To account for the possibility that jets exhibit merging, the average pore spacing $S_a = (N_h(N_h-1))^{-1}\sum_i^{N_h}\sum_{i,j\neq i}^{N_h}(d_{i,j}-2h)$ is considered, where $d_{i,j}$ is the distance between the i^{th} and j^{th} pore. The existence of a relationship between parameter $\xi_f = Re_p N_h \beta^{0.5} S_a D^{-1}$ and C_D is established in Fig.13a, which is attested to be linear for nearly all tested disks. Disks with $\beta = 0.2$, topology A, $\beta = 0.25$, topologies A and C do not follow the predicted trendline defined as $C_D = -0.202 \times 10^{-4} \times \xi_f + 1.25$. These disks did not exhibit a closed near-wake neither, i.e. these disks did not have a rear stagnation point (see Fig.10e).

While deviation of the speculated tendency with ξ_f could be ascribed specifically to the ab-

sence of near-wake closure or strong jet curvature (Figs.6-8 and Fig.10), these anomalies must inherently be related to pore jet spacing as observed in paragraph 3.3. An intricate interplay between pore topology and near-wake flow is hence envisaged to ultimately determine drag. An alternative relationship $\xi_g = N_h^a \beta^b (S_a/D)^c$ is therefore attempted based on the observed dependency of u_p with porosity (Fig.11). Optimal values of -0.125, 1.695 and 0.580 for a, b and c respectively were found. Contrary to ξ_f, parameter ξ_g is uniquely defined by the geometry of the perforated disks and contains no reference to flow parameters such as the Reynolds number. Figure 13b however shows that the variation in the data is not well captured by a linear trendline. The drag coefficient is instead scattered around the linear line, indicating non-linearity, and can attain multiple values for the same ξ_g, implying C_D cannot be predicted based on geometrical considerations alone.

In the case of the solid disk, β and Re_p are zero and the line fits with ξ_f and ξ_g result in a C_D of 1.25 and 1.21 respectively, which is close to that of a solid disk found in related studies. The authors would like to stress that for low disk-based Reynolds numbers, the observed linear tendency with ξ_f will no longer hold as the drag coefficient will display a Reynolds number dependency. For sufficiently large Reynolds numbers however drag coefficients were shown to become independent of Re_D (Fig.5a) and the results currently presented provide, to the best of the authors knowledge, a first time explicit proof of the stipulated interrelation between drag coefficient, perforation layout and Reynolds number.

4 CONCLUSIONS

In this study force measurements, laser Doppler anemometry and Particle Image Velocimetry have been utilized to study the near-wake of perforated disks with different combinations of porosity and perforation topology placed in a smooth airstream at a Reynolds number of 10^5. While it may be obvious that different pore topologies give rise to different near-wake flow patterns and drag coefficients, the extent of the pore topology's influence

and potential tendencies have never been systematically documented. This has been the intention of the current work. To investigate the presence of jet merging among the flow exiting from the pores, simplistic topologies have been considered, each consisting of a series of holes positioned along a single radial location. The paper thus does not provide a comprehensive wake survey behind perforated disks, but is to the best of the authors' knowledge the first to highlight the observed variation in flow topology and drag coefficient due to a decoupled effect of altering hole topology and porosity.

One of the conclusions is that even for the simplistic topologies considered in the current work, it is not possible to predict the drag coefficient or near-wake flow topology solely on the basis of geometrical parameters defining the pore layout. Instead, drag coefficient and wake flow patterns are shown to vary inconsistently with pore layout across the porosities, even producing drag coefficients exceeding that of a solid disk. It was also found that jet merging, whereby all the jets coalesce into one, only appears for sufficiently small intra-pore spacings. Porosity nevertheless remains the dominant parameter influencing drag while pore layout is of secondary importance. For each porosity lowest drag values and largest wake extents were attributed to perforation layouts for which the distance between disk and pore edge was smallest, although this tendency was not identified for highest drag coefficients. It was found that pore jets generally bend outwards to merge with the outer shear-layer and this interaction became stronger as pores were shifted radially outwards. Simultaneously, the wake of each disk showed signs of regular vortex shedding, except for some disks which did not exhibit an enclosed near-wake in the temporally averaged flow field. Conversely, these disks did show signs of regular near-wake pumping in the longitudinal direction, instigating the possibility of so-called multi-stable wake modes. For smallest pore rim-to-rim distances less than 10% of the disk radius, jet merging appeared with a subsequent absence of a rear stagnation point (i.e. well-defined near wake). For all other cases, a tentative linear relationship was established

between the drag coefficient and a parameter involving the ejected flow momentum from the pores, their number and average spacing and overall disk porosity. All wake structures were evidenced to show three-dimensional complexity with categorizable centerline velocity evolutions although none of the wake features could be correlated with a dominant descriptor used to define the pore topologies. Small alterations in topology (predominantly the radial location of the pores) could on the other hand give rise to distinct flow patterns. All entities are thus of importance to fully characterize the influence of perforations as well as their layout on the drag force and wake topology, but it is their influence on the behavior of the outer shear layer that is put forward as being pivotal. The evolution in outer-shear layer due to its interaction with the pore jets warrants further investigation and this will be the subject of future studies.

ACKNOWLEDGMENT

The authors would like to thank Mr. Maximillian Dixon for his assistance during the experimental campaign. Dr Branislav Titurus is especially acknowledged for his aid in the frequency characterization of the test rig.

REFERENCES

[1] Langdon, G., Nurick, G., Balden, V., and Timmis, R., 2008. "Perforated plates as passive mitigation systems". *Defence Science Journal,* **58**(2), pp. 238–247.

[2] Shaaban, S., 2015. "On the performance of perforated plate with optimized hole geometry". *Flow Measurement and Instrumentation,* **46**, pp. 44 – 50.

[3] Malavasi, S., Messa, G., Fratino, U., and Pagano, A., 2012. "On the pressure losses through perforated plates". *Flow Measurement and Instrumentation,* **28**, pp. 57 – 66.

[4] Castro, I. P., 1971. "Wake characteristics of two-dimensional perforated plates normal to an air-stream". *Journal of Fluid Mechanics,* **46**(03), p. 599.

[5] Huang, Z., and Keffer, J. F., 1996. "Development of structure within the turbulent wake of a porous body. part 1. the initial formation region". *Journal of Fluid Mechanics,* **329**(-1), p. 103.

[6] Morel, T., and Bohn, M., 1980. "Flow over two circular disks in tandem". *ASME Journal of Fluids Engineering,* **102**(1), pp. 104–111.

[7] Fouladi, F., Henshaw, P., and Ting, D.-K., 2014. "Turbulent flow over a flat plate downstream of a finite height perforated plate". *ASME Journal of Fluids Engineering,* **137**(2), p. 021203.

[8] Sforza, P., Stasi, W., Smorto, M., and Sheering, P., 1979. "Wind turbine generator wakes". In 17th Aerospace Sciences Meeting (New Orleans, LA, USA).

[9] Lignarolo, L. E. M., Ragni, D., Ferreira, C. J., and van Bussel, G. J. W., 2016. "Experimental comparison of a wind-turbine and of an actuator-disc near wake". *Journal of Renewable and Sustainable Energy,* **8**(2), p. 023301.

[10] Macr, S., Coupiac, O., Girard, N., Leroy, A., and Aubrun, S., 2018. "Experimental analysis of the wake dynamics of a modelled wind turbine during yaw manoeuvres". *Journal of Physics: Conference Series,* **1037**(7), p. 072035.

[11] Yang, X., Boomsma, A., Sotiropoulos, F., Resor, B. R., Maniaci, D. C., and Kelley,

C. L., 2015. “Effects of spanwise blade load distribution on wind turbine wake evolution”. In 33rd Wind Energy Symposium (Kissimmee, Florida, US), p. 0492.

[12] Theunissen, R., Housley, P., Allen, C. B., and Carey, C., 2014. “Experimental verification of computational predictions in power generation variation with layout of offshore wind farms”. *Wind Energy,* **18**(10), pp. 1739–1757.

[13] Cannon, S., Champagne, F., and Glezer, A., 1993. “Observations of large-scale structures in wakes behind axisymmetric bodies”. *Experiments in Fluids,* **14**(6), pp. 447–450.

[14] Perera, M., 1981. “Shelter behind two-dimensional solid and porous fences”. *Journal of Wind Engineering and Industrial Aerodynamics,* **8**(1-2), pp. 93–104.

[15] Higuchi, H., 1991. “Visual study on wakes behind solid and slotted axisymmetric bluff bodies”. *Journal of Aircraft,* **28**(7), pp. 427–430.

[16] Roberts, B. W., 1980. “Drag and pressure distribution on a family of porous, slotted disks”. *Journal of Aircraft,* **17**(6), pp. 393–401.

[17] Svensson, K., Rohdin, P., and Moshfegh, B., 2016. “On the influence of array size and jet spacing on jet interactions and confluence in round jet arrays”. *ASME Journal of Fluids Engineering,* **138**(8), pp. 081206/1–19.

[18] Higuchi, H., Zhang, J., Muzas, B., Furuya, S., Higuchi, H., Zhang, J., Muzas, B., and Furuya, S., 1997. “Experimental study on unsteady flows and multiple near-wake patterns behind slotted disks”. In 14th Aerodynamic Decelerator Systems Technology Conference (San Francisco, CA,USA).

[19] Durve, A., Patwardhan, A. W., Banarjee, I., Padmakumar, G., and Vaidyanathan, G., 2012. “Numerical investigation of mixing in parallel jets”. *Nuclear Engineering and Design,* **242**, pp. 78–90.

[20] Barrett, R., 1984. “Design and performance of a new low turbulence wind tunnel at bristol university”. *The Aeronautical Journal,* **88**(873), pp. 86–90.

[21] Ishizuka, M., and T, H., 2011. "Measurements for flow resistance coefficient values of perforated plates in natural air convection flows". In 8th international conference on heat transfer, fluid mechanics and thermodynamics (Mauritius).

[22] Berger, E., Scholz, D., and Schumm, M., 1990. "Coherent vortex structures in the wake of a sphere and a circular disk at rest and under forced vibrations". *Journal of Fluids and Structures,* **4**(3), pp. 231–257.

[23] Taylor, J., 1997. *Introduction to Error Analysis, the Study of Uncertainties in Physical Measurements, 2nd Edition*. University Science Books, Aug.

[24] Theunissen, R., Sante, A. D., Riethmuller, M. L., and Braembussche, R. A. V. D., 2007. "Confidence estimation using dependent circular block bootstrapping: application to the statistical analysis of piv measurements". *Experiments in Fluids,* **44**(4), pp. 591–596.

[25] Scarano, F., and Riethmuller, M. L., 2000. "Advances in iterative multigrid piv image processing". *Experiments in Fluids,* **29**(7), pp. 51–60.

[26] Westerweel, J., 2000. "Theoretical analysis of the measurement precision in particle image velocimetry". *Experiments in Fluids,* **29**(7), pp. S003–S012.

[27] Hoesel, W., and Rodi, W., 1977. "New biasing elimination method for laserdoppler velocimeter counter processing". *Review of Scientific Instruments,* **48**(7), pp. 910–919.

[28] Gould, R. W. F., 1969. *Wake blockage corrections in a closed wind tunnel for one or two wall-mounted models subject to separated flow*. Reports and memoranda, Ministry of Technology, Aeronautical Research Council. London HMSO.

[29] Maskell, E., and (Great Britain), A. R. C., 1965. *A Theory of the Blockage Effects on Bluff Bodies and Stalled Wings in a Closed Wind Tunnel*. Aeronautical Research Council.

[30] Nobach, H., 2015. "Corrections to the direct spectral estimation for laser doppler

data". *Experiments in Fluids,* **56**(5), May, p. 109.

[31] Benedict, L. H., Nobach, H., and Tropea, C., 2000. "Estimation of turbulent velocity spectra from laser doppler data". *Measurement Science and Technology,* **11**(8), pp. 1089–1104.

[32] Velte, C. M., George, W. K., and Buchhave, P., 2014. "Estimation of burst-mode lda power spectra". *Experiments in Fluids,* **55**(3), Mar, p. 1674.

[33] Scott, D. W., 2009. "Averaged shifted histogram". *Wiley Interdisciplinary Reviews: Computational Statistics,* **2**(2), pp. 160–164.

[34] Craze, D., 1977. "On the near wake behind a circular disc". In 6th Australasian hydraulics and fluid mechanics conference (Adelaide, Australia), pp. 282–286.

[35] Blackmore, T., Batten, W. M. J., Műller, G. U., and Bahaj, A. S., 2013. "Influence of turbulence on the drag of solid discs and turbine simulators in a water current". *Experiments in Fluids,* **55**(1), Dec, p. 1637.

[36] Taylor, G. I., and (Great Britain), A. R. C., 1944. *The aerodynamics of porous sheets*. Aeronautical Research Council.

[37] Tanaka, E., 1974. "The interference of two-dimensional parallel jets : 2nd report, experiments on the combined flow of dual jet". *Bulletin of JSME,* **17**(109), pp. 920–927.

[38] Lin, Y. F., and Sheu, M. J., 1990. "Investigation of two plane parallel unventilated jets". *Experiments in Fluids,* **10**(1), pp. 17–22.

[39] Villermaux, E., and Hopfinger, E. J., 1994. "Periodically arranged co-flowing jets". *Journal of Fluid Mechanics,* **263**(-1), p. 63.

[40] Nedić, J., Ganapathisubramani, B., and Vassilicos, J. C., 2013. "Drag and near wake characteristics of flat plates normal to the flow with fractal edge geometries". *Fluid Dynamics Research,* **45**(6), p. 061406.

[41] Anderson, E. A., Snyder, D. O., and Christensen, J., 2002. "Experimental investi-

gation of periodic behavior between parallel planar jets". In 40th AIAA Aerospace Sciences Meeting and Exhibit (Reno, NV, USA).

[42] Yang, J., Liu, M., Wu, G., Zhong, W., and Zhang, X., 2014. "Numerical study on coherent structure behind a circular disk". *Journal of Fluids and Structures,* **51**, pp. 172–188.

[43] Miau, J. J., Leu, T. S., Liu, T. W., and Chou, J. H., 1997. "On vortex shedding behind a circular disk". *Experiments in Fluids,* **23**(3), pp. 225– 233.

[44] Lee, S., and Bearman, P., 1992. "An experimental investigation of the wake structure behind a disk". *Journal of Fluids and Structures,* **6**(4), pp. 437– 450.

[45] Kiya, M., Ishikawa, H., and Sakamoto, H., 2001. "Near-wake instabilities and vortex structures of three-dimensional bluff bodies: a review". *Journal of Wind Engineering and Industrial Aerodynamics,* **89**(14-15), pp. 1219– 1232.

[46] Zhong, W., Liu, M., Wu, G., Yang, J., and Zhang, X., 2014. "Extraction and recognization of large-scale structures in the turbulent near wake of a circular disc". *Fluid Dynamics Research,* **46**(2), p. 025507.

[47] Tian, X., Ong, M. C., Yang, J., and Myrhaug, D., 2016. "Large-eddy simulations of flow normal to a circular disk at $Re = 1.5 \times 10^5$". *Computers and Fluids,* **140**(Supplement C), pp. 422 – 434.

[48] Roberts, J., 1973. "Coherence measurements in an axisymmetric wake". *AIAA Journal,* **11**(11), pp. 1569–1571.

[49] Fey, U., Knig, M., and Eckelmann, H., 1998. "A new Strouhal-Reynolds-number relationship for the circular cylinder in the range $47 < Re < 2 \times 10^5$". *Physics of Fluids,* **10**(7), pp. 1547–1549.

[50] Vanierschot, M., Dyck, K. V., Sas, P., and den Bulck, E. V., 2014. "Symmetry breaking and vortex precession in low-swirling annular jets". *Physics of Fluids,* **26**(10), pp. 105–110.

[51] Bunderson, N. E., and Smith, B. L., 2005. "Passive mixing control of plane parallel jets". *Experiments in Fluids,* **39**(1), pp. 66–74.

[52] Sanmiguel-Rojas, E., Sevilla, A., Martnez-Bazn, C., and Chomaz, J.-M., 2009. "Global mode analysis of axisymmetric bluff-body wakes: Stabilization by base bleed". *Physics of Fluids,* **21**(11), p. 114102.

[53] Gentile, V., Schrijer, F. F. J., Van Oudheusden, B. W., and Scarano, F., 2016. *Organization of an Axisymmetric Turbulent Wake in Presence of a Central Protrusion*. Springer International Publishing, Cham, pp. 157–163.

APPENDIX: SINGLE-AXIS DRAG MEASUREMENT

The drag was evaluated by means of a single component load cell of length L, Young's modulus E and moment of inertia I around the bending axis x converting local bending into voltage through a strain-gauge (Fig. 14). In the following it is shown that this is a valid procedure considering time-averaged data. The load acting on the support structure during wind tunnel testing is considered to be taken into consideration by subtracting the related drag force. This constitutes a first-order correction but can be considered sufficient given the small size of the support.

Calibrations were performed applying known point loads F_c to the center of the disk with diameter D and recording the voltages V_c (Fig. 14a);

$$V_c \propto F_c \frac{L^3}{3EI} + \underbrace{F_c \frac{D}{2}}_{=M_c} \frac{L^2}{2EI} = \frac{F_c L^2}{6EI}(2L + 3D/2) \tag{6}$$

Without loss of generality, the problem is reduced to one dimension hereafter for clarity. The instantaneous pressure distribution $f(y,t)$ is analogous to a point load $F(t) = \int f(y,t)dy$ acting at a distance $Y(t) = \int f(y,t)ydy/F(t)$ and thus introducing a moment $M(t)$ (Fig. 14b). The load $F(t)$ does not necessarily act at the center of the disk, but can exhibit a precession (e.g. [53]). Both quantities are therefore decomposed into a mean and fluctuating component; $F(t) = \overline{F} + F'(t)$, $Y(t) = D/2 + Y'(t)$. Substitution in the instantaneous voltage and time-averaging over a time T yields

$$\overline{V} \propto \overline{F}\frac{L^3}{3EI} + \overline{F}\frac{D}{2}\frac{L^2}{2EI} + \frac{L^2}{2EI}\underbrace{\frac{1}{T}\int F'(t)Y('t)dt}_{\overline{\epsilon}} \tag{7}$$

In estimating the drag force, the force $\overline{F^*}$ is sought producing a voltage, based on the performed calibration (Eqn.6), equal to the obtained $\overline{V}$ (viz. Eqn.7); $\overline{F^*} = \overline{F} + \overline{\epsilon}\frac{6}{4L+3D}$. The term $\overline{\epsilon}$ represents the time average of $\epsilon = F'(t)Y'(t)$ and, in line with ergodicity, the expected value $\mathbf{E}$; $\overline{\epsilon} = \frac{1}{T}\int F'(t)Y'(t)dt = \mathbf{E}(\epsilon) = \int \epsilon\rho(\epsilon)d\epsilon$ where ρ represents the probability density function of ϵ. As the disks exhibit azimuthal symmetry, the resulting drag force $\overline{F}$ will act at the center of the disks (all disks tested were of equal diameter D and exhibited geometrical symmetry along the x and y axes, implying symmetry in the load; $f(x,y) = f(|x|,|y|)$), implying the probability distribution of $Y'(t)$ to be symmetric. This is confirmed by the data of Gentile *et al.* [53] and the numerical data of Yang *et al.* [42]. In the latter it was also shown that the probability distribution of $F'(t)$ was symmetric. With symmetric $\rho(Y')$ and $\rho(F')$, so will $\rho(\epsilon)$. As such, $\mathbf{E}(\epsilon) = 0 = \overline{\epsilon}$ and $\overline{F^*} \equiv \overline{F}$ proving that a single-axis load cell can be used to retrieve the time-average drag force provided T is sufficiently large. In the current experiments, approximately 1900 samples were recorded over a total time of 60 seconds ensuring statistical convergence.

It should be noted that in terms of the fluctuating force component, one obtains $F^{*\prime}(t) = F'(t) + \left(\overline{F}Y'(t) + F'(t)Y'(t)\right)\frac{6}{4L+3D}$. This implies that when using the calibrated relation between voltage and force, the fluctuation in derived drag force is not solely related to the actual drag fluctuation, but comprises also the fluctuations $Y'(t)$. However, the standard deviation in $F^{*\prime}$, measured through the data spread, will clearly be larger than the standard deviation of solely $F'(t)$. This only strengthens the argument made within the current work that the observed variation in drag coefficient within one porosity class is not due to

measurement uncertainty, but caused by perforation alterations.

TABLES

LIST OF TABLES

Table 1: Overview of the geometrical parameters defining the perforated disks. Disks with porosities $\beta = 0.05$, 0.10, 0.20 and 0.25 were selected for further LDA surveys. Dark gray rows indicate excluded disk topologies due to unphysical parameter values ($S - 2h \leq 0$). Light gray cells indicate the disk types exhibiting pore jet merging. Underlined values link disks of equal S/h.

		$\beta = 0.05$				$\beta = 0.10$			
Topology	N_h	r_p/R	h/R	S/R	S/h	r_p/R	h/R	S/R	S/h
A	4	0.36	0.11	0.51	4.59	0.36	0.16	0.51	3.25
B	6	0.36	0.09	0.36	3.97	0.36	0.13	0.36	2.81
C	4	0.41	0.11	0.58	5.22	0.41	0.16	0.58	3.69
D	4	0.46	0.11	0.65	5.86	0.46	0.16	0.65	4.14
E	4	0.51	0.11	0.73	6.49	0.51	0.16	0.73	4.59
F	6	0.51	0.09	0.51	5.62	0.51	0.13	0.51	3.97

		$\beta = 0.20$				$\beta = 0.25$			
Topology	N_h	r_p/R	h/R	S/R	S/h	r_p/R	h/R	S/R	S/h
A	4	0.36	0.22	0.51	2.29	0.36	0.25	0.51	2.05
B	6	0.36	0.18	0.36	1.99	0.36	0.20	0.36	1.78
C	4	0.41	0.22	0.58	2.61	0.41	0.25	0.58	2.34
D	4	0.46	0.22	0.65	2.93	0.46	0.25	0.65	2.62
E	4	0.51	0.22	0.73	3.25	0.51	0.25	0.73	2.90
F	6	0.51	0.18	0.51	2.81	0.51	0.20	0.51	2.51

		$\beta = 0.30$				$\beta = 0.35$			
Topology	N_h	r_p/R	h/R	S/R	S/h	r_p/R	h/R	S/R	S/h
A	4	0.36	0.27	0.51	1.87	0.36	0.30	0.51	1.73
B	6	0.36	0.22	0.36	1.62	0.36	0.24	0.36	1.50
C	4	0.41	0.27	0.58	2.13	0.41	0.30	0.58	1.97
D	4	0.46	0.27	0.65	2.39	0.46	0.30	0.65	2.21
E	4	0.51	0.27	0.73	2.65	0.51	0.30	0.73	2.45
F	6	0.51	0.22	0.51	2.29	0.51	0.24	0.51	2.12

		$\beta = 0.50$			
Topology	N_h	r_p/R	h/R	S/R	S/h
A	4	0.36	0.35	0.51	1.45
B	6	0.36	0.29	0.36	1.26
C	4	0.41	0.35	0.58	1.65
D	4	0.46	0.35	0.65	1.85
E	4	0.51	0.35	0.73	2.05
F	6	0.51	0.29	0.51	1.78

Table 2: Drag coefficient for porous disks of varying porosity and hole topology. Bold values indicate for each porosity the highest C_D across the topologies, underlined the lowest. Symbols and markers correspond with data depicted in Fig.5.

	Pore topology					
β	A	B	C	D	E	F
0.05	1.218	**1.235**	1.219	1.224	1.191	1.221
0.10	1.187	1.186	**1.198**	1.181	1.145	1.161
0.20	1.139		**1.144**	1.109	1.079	1.122
0.25	1.047		**1.093**	1.086	1.037	1.051
0.30			1.028	**1.067**	1.086	1.038
0.35				**1.008**	0.969	0.996
0.50					**0.707**	

Table 3: Location of the merging/rear-stagnation point, normalized with disk diameter (cf. Fig.10f). Bold and underlined values indicate for each porosity respectively the largest and smallest near-wake extent.

	Pore topology						
β	Solid	A	B	C	D	E	F
0 (Solid)	**2.476**						
0.05		2.433	2.318	2.401	2.418	**2.442**	2.382
0.10		2.283	2.185	2.358	**2.408**	2.405	2.331
0.20		–		1.991	2.083	**2.172**	2.002
0.25		–		–	1.756	1.921	**2.341**

FIGURES

LIST OF FIGURES

1 (a) Proposed hole topologies for groups of constant porosity. (b) Visual definition of geometric perforated disk parameters.

2 (a) Disk and load cell arrangement for force measurements. (b) LDA centerline measurements. (c) Disk mount in the test section of the University of Bristols low turbulence wind tunnel. (d) PIV setup.

3 Schematics depicting (a) the orientation of the diagonal, vertical and across PIV measurement planes together with (b) the adopted coordinate systems.

4 Analysis of LDA data along the centerline downstream of the solid disk. (a) Spectra in the horizontal u and vertical v velocity component 1.0 and 2.5 diameters downstream. (b) Evolution in Strouhal number St related to the dominant spectral peaks. (c) Corresponding probability distributions in Strouhal number. The length of the vertical gray lines, which indicate the location of 75% peak height, is used as error heuristic for Strouhal number estimations.

5 (a) Evolution in drag coefficient with (a) Reynolds numbers and (b) reciprocal of porosity for perforated disks of varying β and hole topology. The gray band indicates the error band for the solid disk ($C_D = 1.167$).

6 Mean longitudinal velocity fields and streamline pattern obtained with PIV. Left column: vertical plane, middle column: across, left column: diagonal (cf. Fig.3). (a)-(c) $\beta = 0.05$, topology A. (d)-(f) $\beta = 0.05$, topology D. (g)-(i) $\beta = 0.05$, topology E.

7 Mean longitudinal velocity fields and streamline pattern obtained with PIV. Left column: vertical plane, middle column: across, left column: diagonal (cf. Fig.3). (a)-(c) $\beta = 0.10$, topology B. (d)-(f) $\beta = 0.10$, topology F. (g)-(i) $\beta = 0.20$, topology A.

8 Mean longitudinal velocity fields and streamline pattern obtained with PIV. Left column: vertical plane, middle column: across, left column: diagonal (cf. Fig.3). (a)-(c) $\beta = 0.25$, topology A. (d)-(f) $\beta = 0.25$, topology E. (g) Solid.

9 Mean longitudinal velocity profiles extracted in the vertical (a,b) and across (c,d) PIV planes. Dash-dotted lines in the across planes (b,d) connect the velocity peaks along the downstream locations indicating jets to be curved inwards or outwards. The horizontal dashed lines in the across planes indicate the geometrical limits of the disks, given by $\frac{\eta}{R} = \pm\sqrt{1 - r_p^2 R^{-2} \cos^2\left(\pi N_h^{-1}\right)}$; $\frac{\eta}{D} = \pm 0.472$ (A), ± 0.475 (B), ± 0.483 (D), ± 0.455 (E), ± 0.448 (F). Pores in the vertical plane are located at $r/D = \pm r_p/D$ and $\eta/D = \pm\frac{1}{2}S/D$ across.

10 Identified perforated disk near-wake flow regimes based on sequential longitudinal velocity along disk centerlines. Symbolic flow evolution (Flow direction; +: forward, -: reverse. Velocity gradient; $>$: decelerating, =: constant, $<$: accelerating); (a) $-<$, $->$, $+<$ (b) $+>$, $-<$, $->$, $+<$ (c) $-=$, $->$, $+<$ (d) $->$, $+<$ (e) $+>$, $+>$, ($-<$, $->$, if $\beta = 0.10$, A), $+<$ (f) Evolution in merging/rear-stagnation point with porosity (cf. Tab. 3). Error bars relate to the measured standard deviation in velocity ($\pm\sqrt{\overline{u'^2}}$) and translate to errors at 95% confidence level when multiplied by a factor 1.96/ $\sqrt{8000}$.

11 Variation in pore exit velocity with disk porosity for the various perforation topologies. Data was captured at $X/D = 0.3$. Error bars are derived from horizontal turbulence intensity levels. Symbols have been slightly offset in the horizontal direction for clarity.

12 Evolution in Strouhal number St based on (a) the longitudinal ($u; St_u$) and (b) the transversal ($v; St_v$) velocity component measured along the center-line of disks of varying porosity and hole topology. Symbols have been offset in the horizontal direction for clarity. Marker sizes are proportional to the probability of indicated Strouhal number relative to the probability of the dominating peak (Fig.4). Colors correspond to the different porosities as is the case in preceding figures. Gray bands are associated to the natural frequency of the test rig.

13 Variation in drag coefficient with (a) proposed parameter ξ_f incorporating pore Reynolds number Re_p based on data presented in Fig.11, number of holes N_h, average hole spacing S_a and porosity β (b) proposed parameter ξ_g implicating solely geometric quantities.

14 Free-body diagram of the load cell (a) during calibration (b) during instantaneous drag measurements.

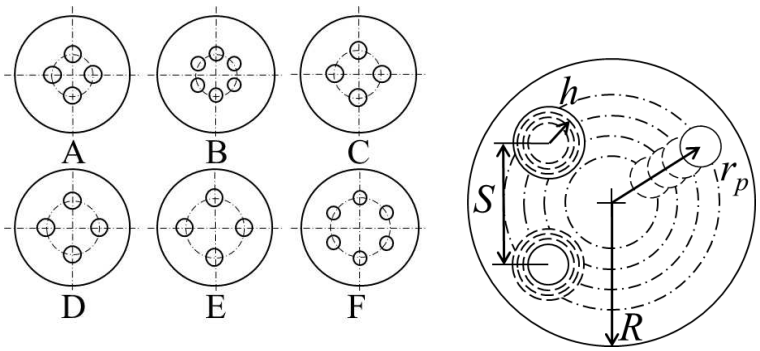

(a) (b)

Fig. 1: (a) Proposed hole topologies for groups of constant porosity. (b) Visual definition of geometric perforated disk parameters.

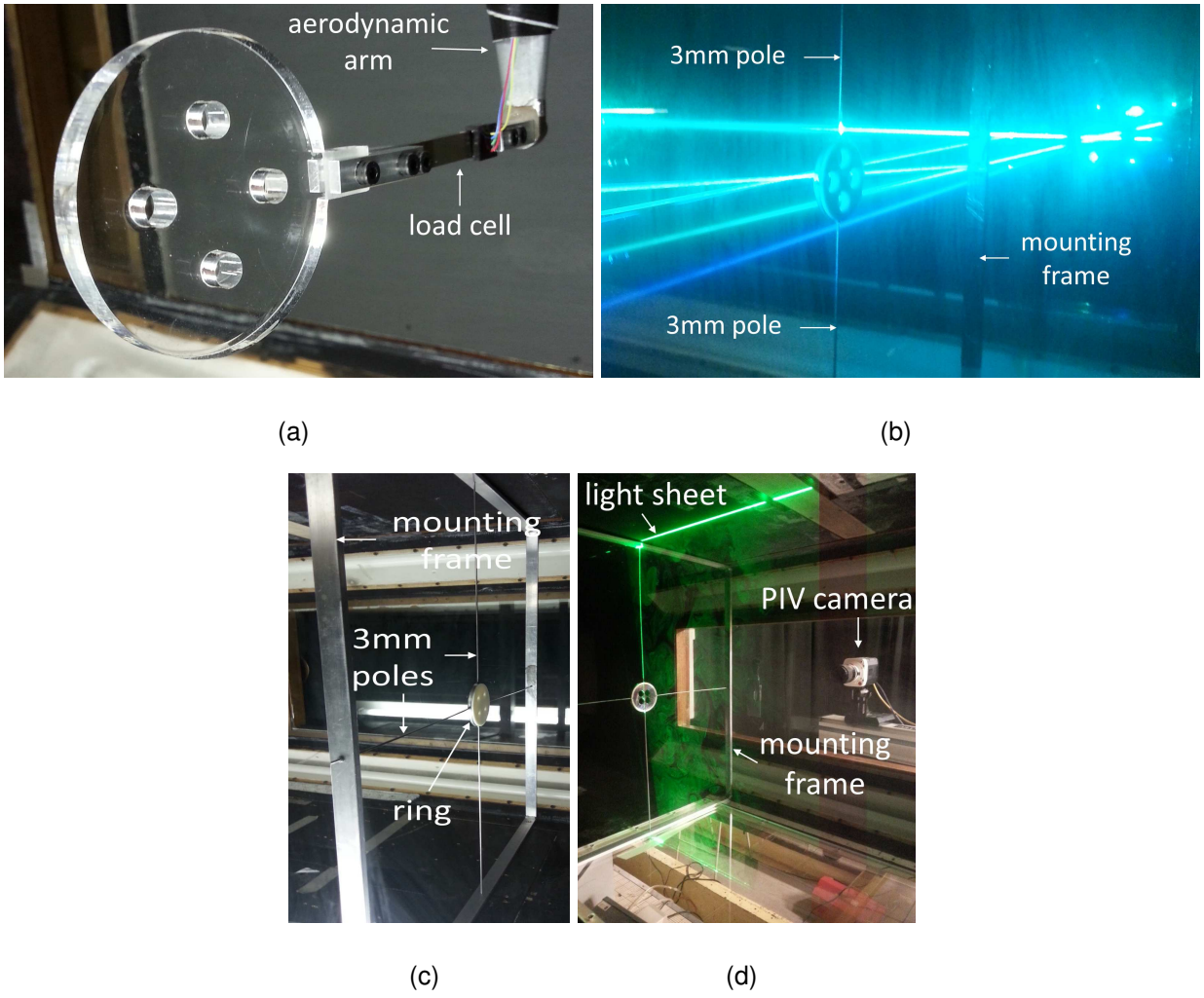

Fig. 2: (a) Disk and load cell arrangement for force measurements. (b) LDA centerline measurements. (c) Disk mount in the test section of the University of Bristols low turbulence wind tunnel. (d) PIV setup.

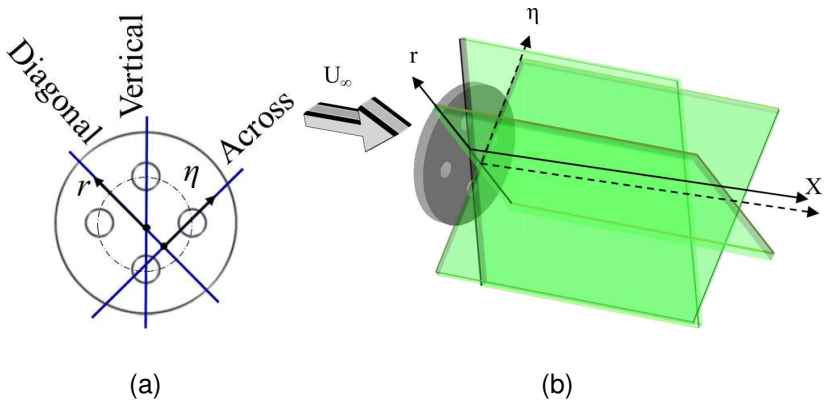

Fig. 3: Schematics depicting (a) the orientation of the diagonal, vertical and across PIV measurement planes together with (b) the adopted coordinate systems.

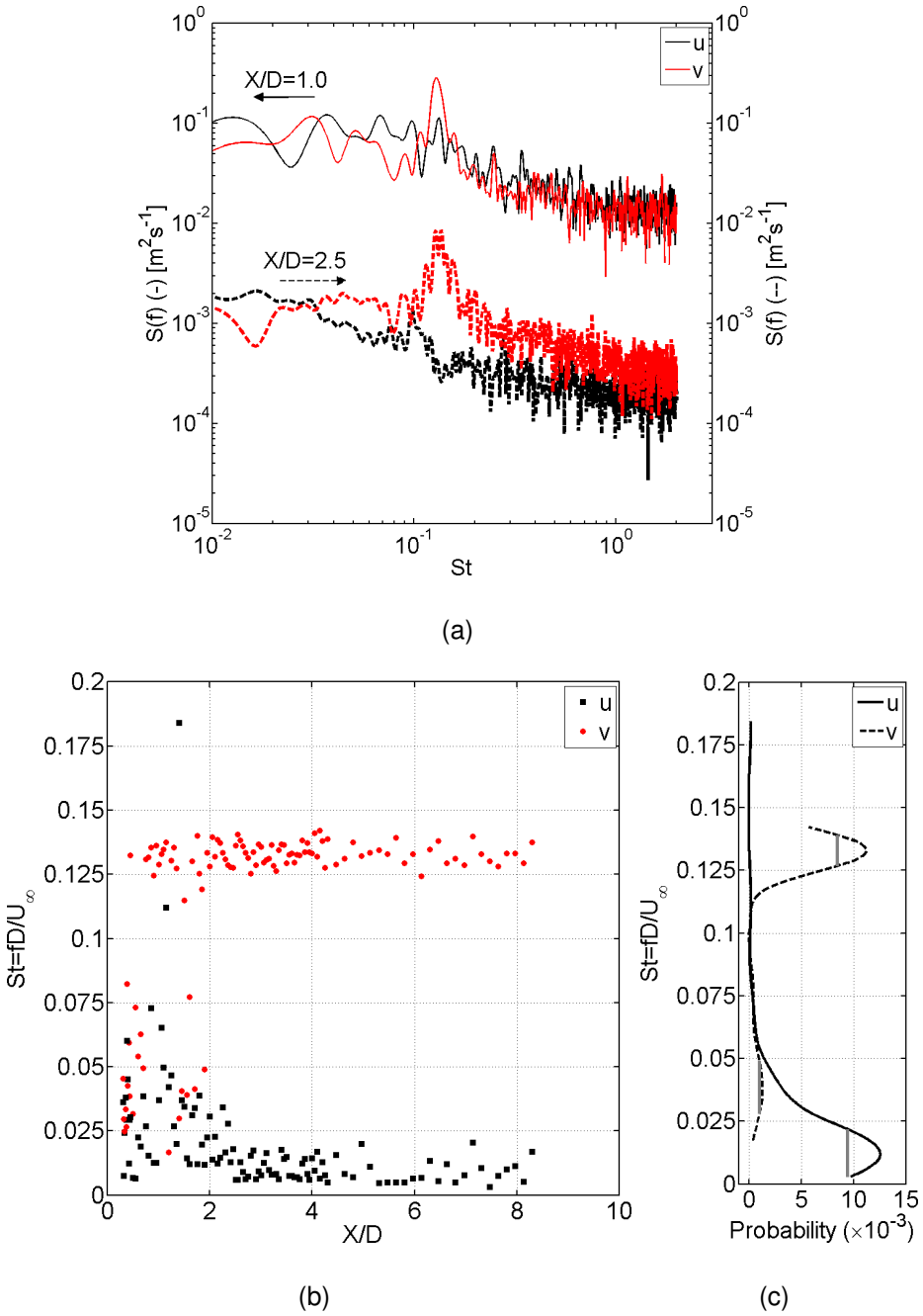

Fig. 4: Analysis of LDA data along the centerline downstream of the solid disk. (a) Spectra in the horizontal u and vertical v velocity component 1.0 and 2.5 diameters downstream. (b) Evolution in Strouhal number St related to the dominant spectral peaks. (c) Corresponding probability distributions in Strouhal number. The length of the vertical gray lines, which indicate the location of 75% peak height, is used as error heuristic for Strouhal number estimations.

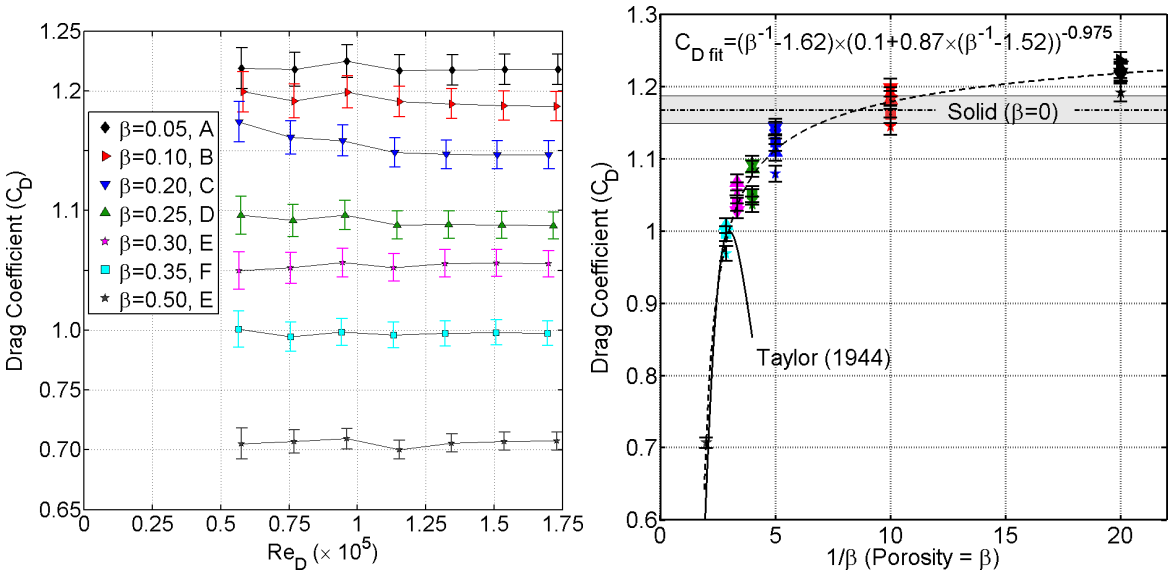

(a) (b)

Fig. 5: (a) Evolution in drag coefficient with (a) Reynolds numbers and (b) reciprocal of porosity for perforated disks of varying β and hole topology. The gray band indicates the error band for the solid disk ($C_D = 1.167$).

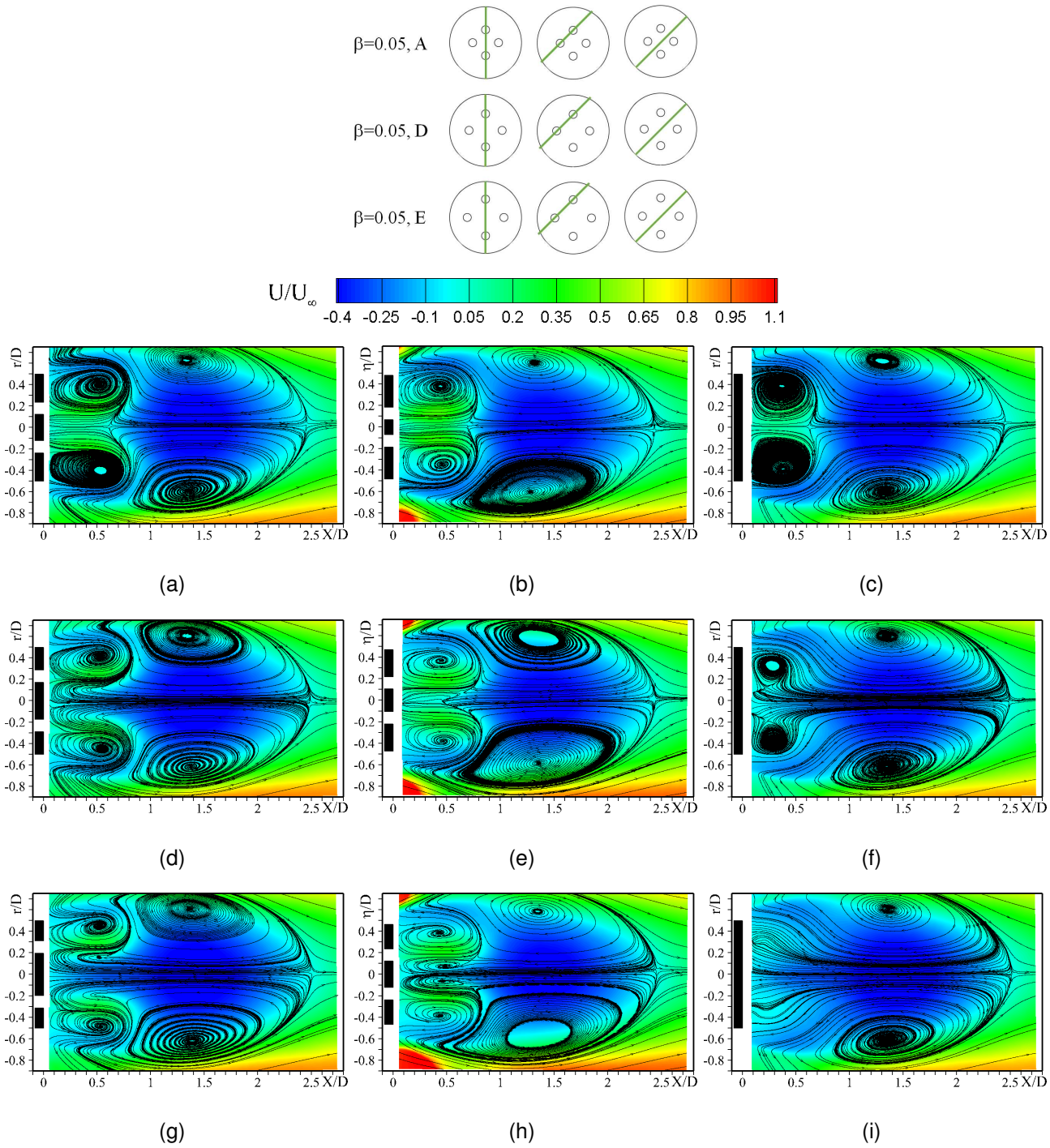

Fig. 6: Mean longitudinal velocity fields and streamline pattern obtained with PIV. Left column: vertical plane, middle column: across, left column: diagonal (cf. Fig.3). (a)-(c) $\beta = 0.05$, topology A. (d)-(f) $\beta = 0.05$, topology D. (g)-(i) $\beta = 0.05$, topology E.

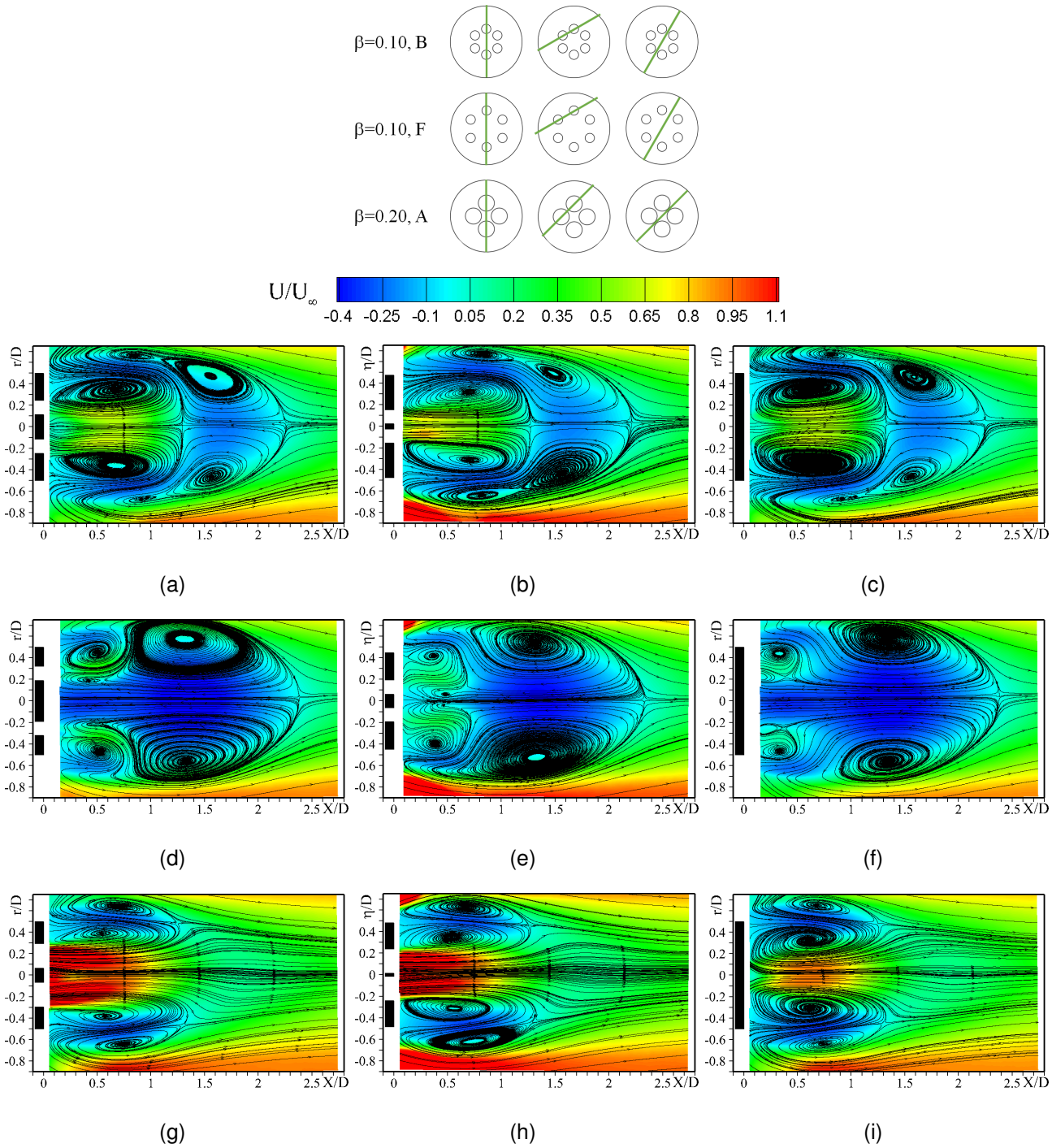

Fig. 7: Mean longitudinal velocity fields and streamline pattern obtained with PIV. Left column: vertical plane, middle column: across, left column: diagonal (cf. Fig.3). (a)-(c) $\beta = 0.10$, topology B. (d)-(f) $\beta = 0.10$, topology F. (g)-(i) $\beta = 0.20$, topology A.

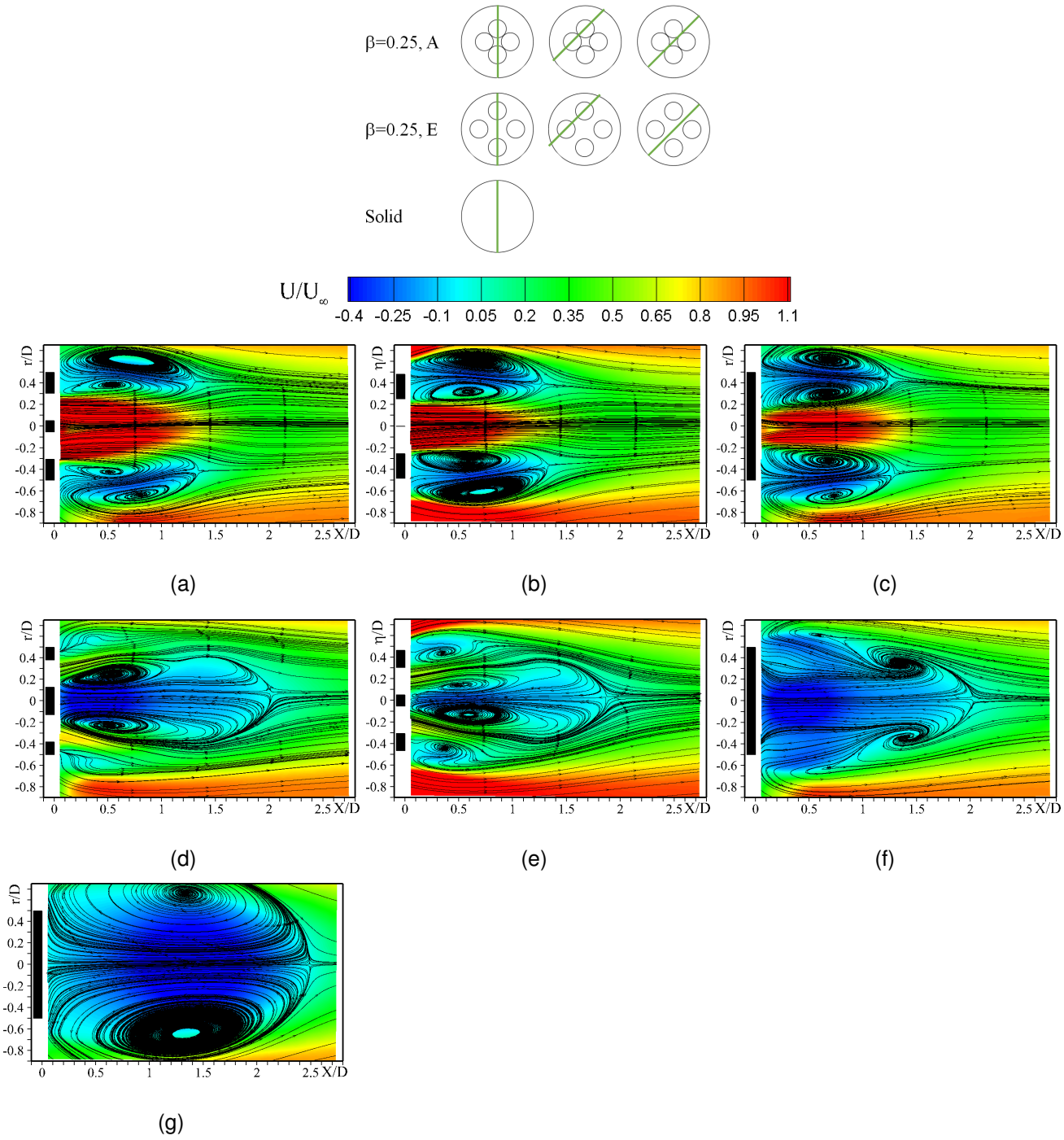

Fig. 8: Mean longitudinal velocity fields and streamline pattern obtained with PIV. Left column: vertical plane, middle column: across, left column: diagonal (cf. Fig.3). (a)-(c) $\beta = 0.25$, topology A. (d)-(f) $\beta = 0.25$, topology E. (g) Solid.

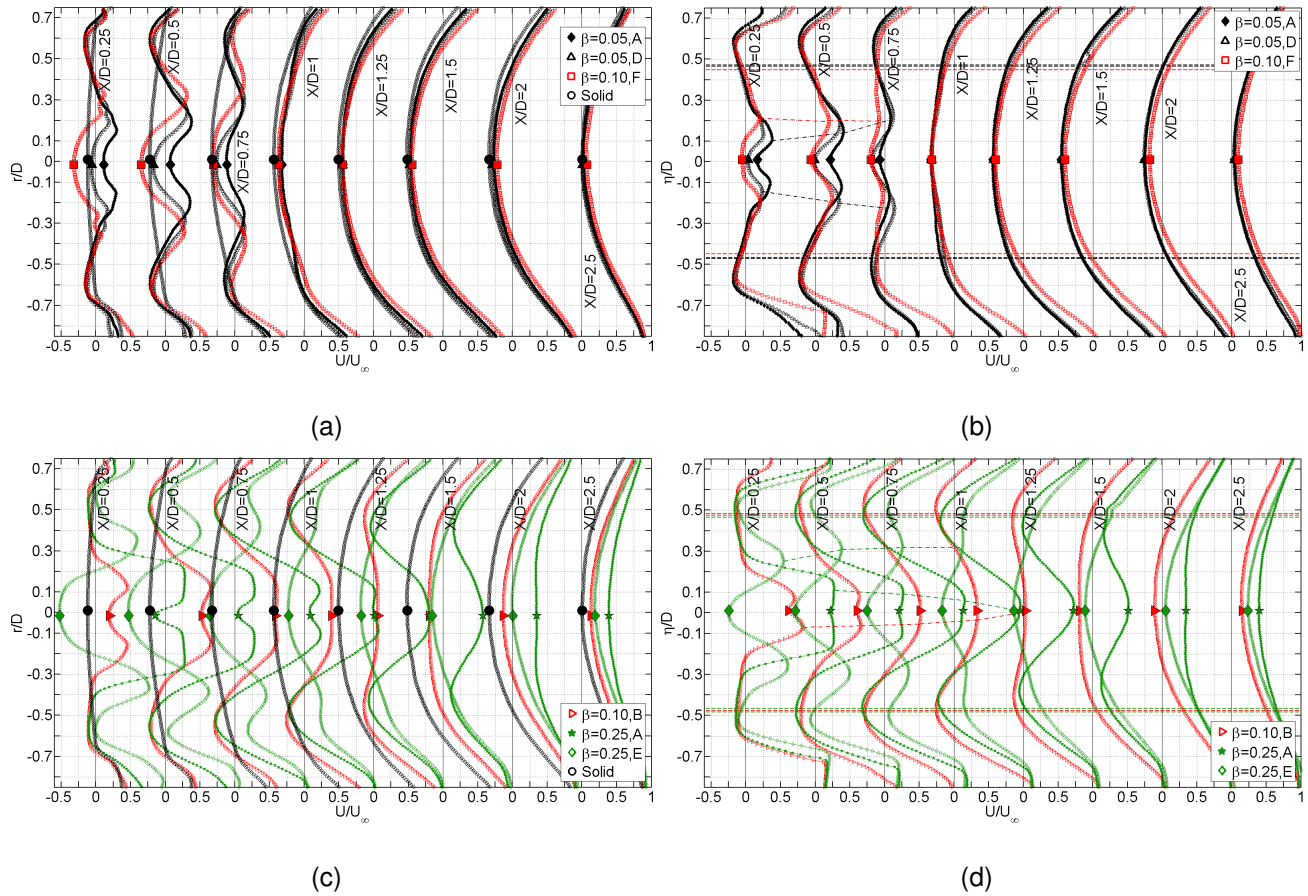

Fig. 9: Mean longitudinal velocity profiles extracted in the vertical (a,b) and across (c,d) PIV planes. Dash-dotted lines in the across planes (b,d) connect the velocity peaks along the downstream locations indicating jets to be curved inwards or outwards. The horizontal dashed lines in the across planes indicate the geometrical limits of the disks, given by $\frac{\eta}{R} = \pm\sqrt{1 - r_p^2 R^{-2} \cos^2\left(\pi N_h^{-1}\right)}$; $\frac{\eta}{D} = \pm 0.472$ (A), ± 0.475 (B), ± 0.483 (D), ± 0.455 (E), ± 0.448 (F). Pores in the vertical plane are located at $r/D = \pm r_p/D$ and $\eta/D = \pm\frac{1}{2}S/D$ across.

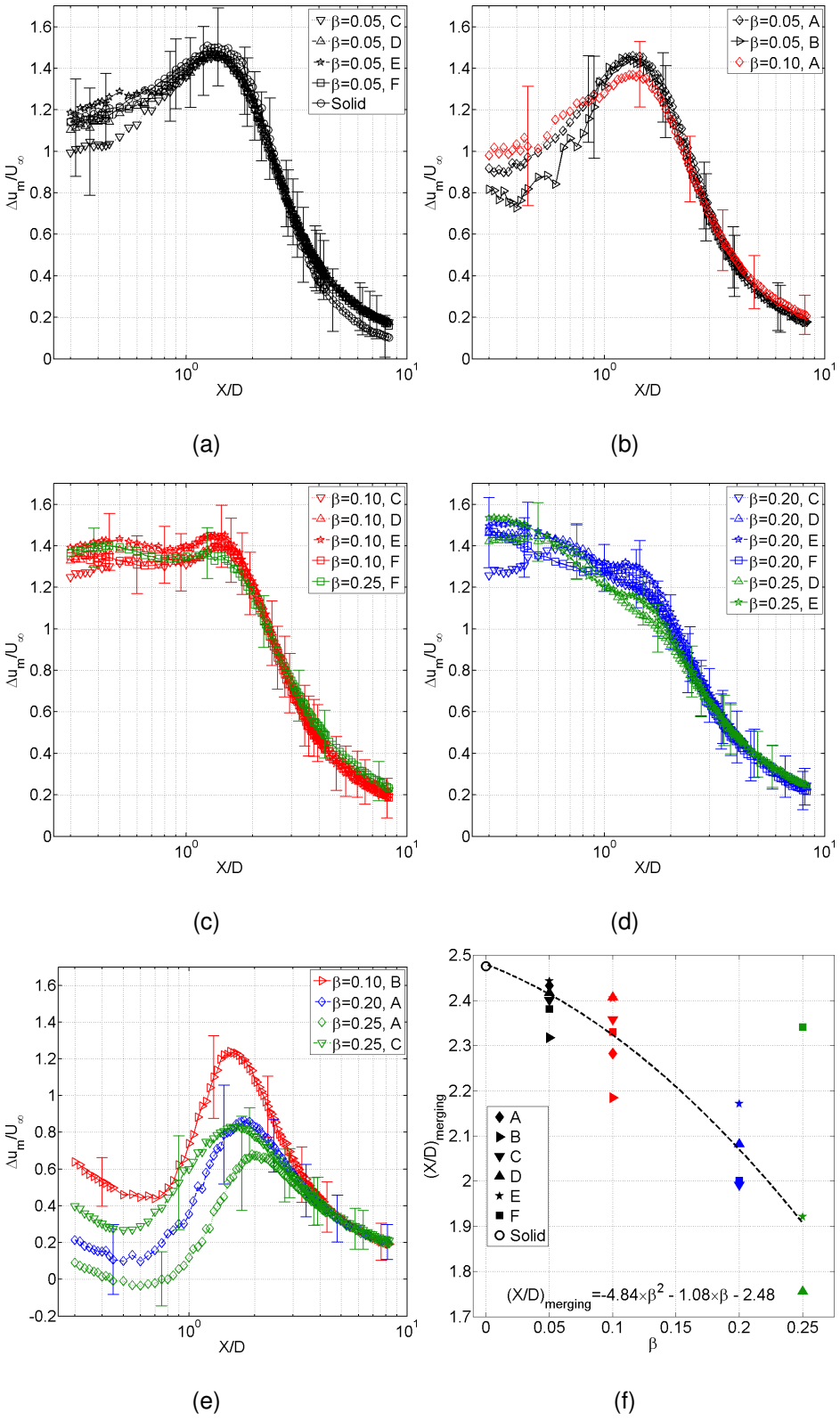

Fig. 10: Identified perforated disk near-wake flow regimes based on sequential longitudinal velocity along disk centerlines. Symbolic flow evolution (Flow direction; +: forward, -: reverse. Velocity gradient; $>$: decelerating, $=$: constant, $<$: accelerating); (a) $-<$, $->$, $+<$ (b) $+>$, $-<$, $->$, $+<$ (c) $-=$, $->$, $+<$ (d) $->$, $+<$ (e) $+>$, $+>$, ($-<$, $->$, if $\beta = 0.10$, A), $+<$ (f) Evolution in merging/rear-stagnation point with porosity (cf. Tab. 3). Error bars relate to the measured standard deviation in velocity ($\pm\sqrt{\overline{u'^2}}$) and translate to errors at 95% confidence level when multiplied by a factor $1.96/\sqrt{8000}$.

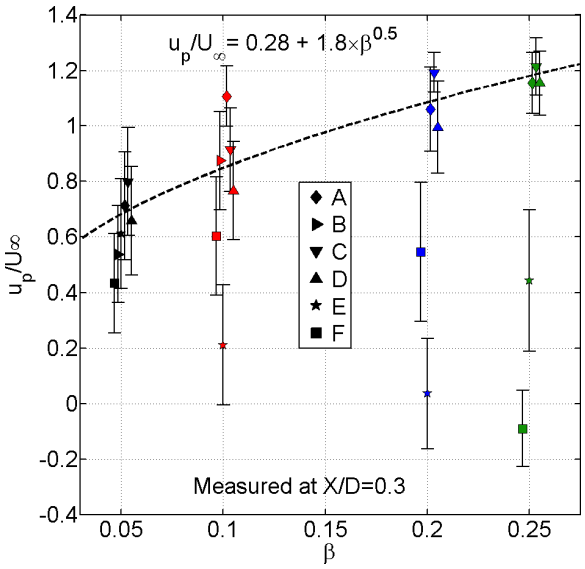

Fig. 11: Variation in pore exit velocity with disk porosity for the various perforation topologies. Data was captured at $X/D = 0.3$. Error bars are derived from horizontal turbulence intensity levels. Symbols have been slightly offset in the horizontal direction for clarity.

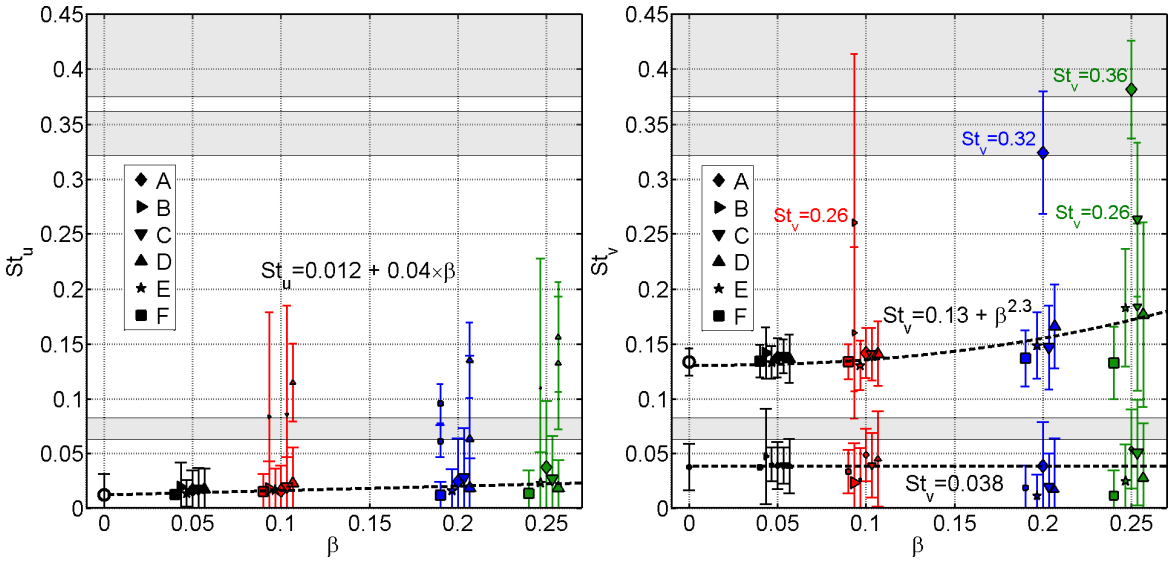

(a) (b)

Fig. 12: Evolution in Strouhal number St based on (a) the longitudinal $(u; St_u)$ and (b) the transversal $(v; St_v)$ velocity component measured along the centerline of disks of varying porosity and hole topology. Symbols have been offset in the horizontal direction for clarity. Marker sizes are proportional to the probability of indicated Strouhal number relative to the probability of the dominating peak (Fig.4). Colors correspond to the different porosities as is the case in preceding figures. Gray bands are associated to the natural frequency of the test rig.

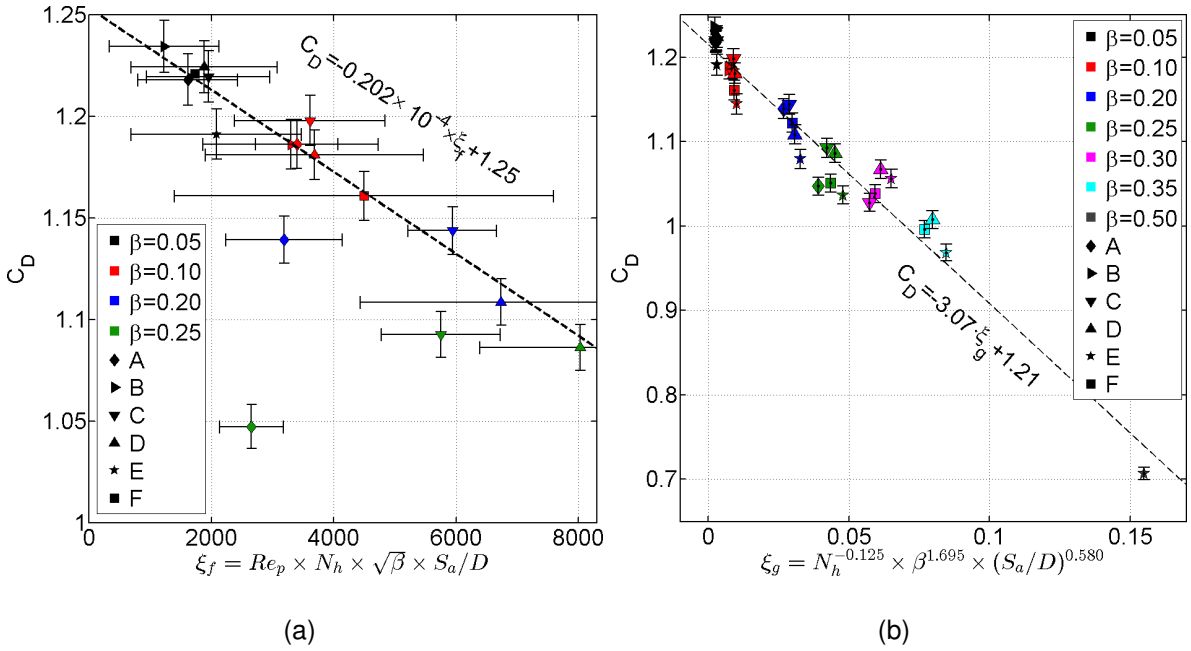

(a) (b)

Fig. 13: Variation in drag coefficient with (a) proposed parameter ξ_f incorporating pore Reynolds number Re_p based on data presented in Fig.11, number of holes N_h, average hole spacing S_a and porosity β (b) proposed parameter ξ_g implicating solely geometric quantities.

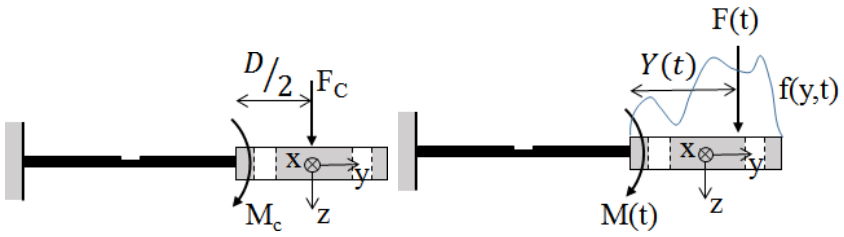

(a) (b)

Fig. 14: Free-body diagram of the load cell (a) during calibration (b) during instantaneous drag measurements.